GRAVITY CURRENT AND AIR POCKET ENTRAPMENTS CAUSED BY SHEAR-FLOW INSTABILITIES IN RAPID-FILLING PIPES

by

Yasemin Eldayih

A thesis submitted to the Graduate Faculty of
Auburn University
in partial fulfillment of the requirements for the Degree of
Master of Science
Auburn, Alabama
December 15, 2018

Keywords:
Air-Water Interaction, Shear Flow Instability, Air-pocket Entrapment, Gravity Current

Approved by
Jose Vasconcelos, Associate Professor of Civil Engineering
Xing Fang, Chair, Arthur H. Feagin Chair Professor of Civil Engineering
Frances O'Donnell, Assistant Professor of Civil Engineering

Abstract

Understanding the behavior of air-water interactions in closed conduits is very important for urban water systems that are subject to rapid filling conditions, such as stormwater systems during intense rain events. Among different mechanisms for air pocket appearance in closed conduits, shear flow instability is one that has significant capability to capture large volumes of air. Upon capture, air phase influences surging and, upon uncontrolled release, lead to issues such as manhole cover displacement and/or geysering. This work presents experimental and numerical research on air pocket entrapment based on shear flow instabilities. A fully-filled horizontal water pipe was opened at the downstream end and creates a cavity flow. After some advance within the pipe, a second valve was maneuvered at the upstream end, enabling pressurized flows from the upstream end. The pipe-filling bore that was created pushed air in high velocity over the air cavity. In some cases, air pocket entrapment followed leading to pressure peaks appear to be characteristic of this type of entrapment. In the numerical part, an CFD model with the same scale of the experimental apparatus was implemented alongside with a larger-scale model ten times larger than the experimental scale. Results comparison showed that CFD predicts air pocket formation more frequently than comparable experiments. CFD results were also compared to and matched well with the theoretical instability threshold formulas. Overall, useful results for the future investigations of air-pocket entrapments caused by shear flow instabilities in the stormwater systems was obtained to help to solve many operational problems.

Acknowledgments

I would like to acknowledge for support of the General Directorate of State Hydraulic Works (DSI) under Republic of Turkey Ministry of Forestry and Water Affairs, which has provided a fellowship to me with the grand number of 33070922-772.02-736534 for my graduate study in the US.

I greatly appreciate my advisor Dr. Jose Vasconcelos for his continuous support, encouragement, kindness, patience and for everything he has done for me during my research and the life in the U.S. I will never be able to thank him enough for touching my life and guide me to the person I became.

I greatly appreciate Dr. Xing Fang and Dr. Frances O'Donnell for being my committee members. I also would like to thank Dr. Latif Kalin, Prabhakar Clement that I took courses and learnt a lot.

I want to thank specially Recep Tayyip Kanber for his effort and support since January 2015 that was the time we have first met and earned the scholarship from Turkish government.

I also would like to thank my friends in Auburn especially Jalil Ahmad Jamily who became a second advisor and a brother to me in the past two years and shared his experience about engineering and life with me generously. Although Auburn is a small city, friendship means forever and always warm in Auburn. I would like to thank Gokhan Ucar, Halil Ibrahim Kurt, Abdullah Hanar, Willilam Song, Alev Guven, Sama Sheykhmemari, Dawood Hafizy, Sagar

Tamang, Sudan Pokharel, Zuhier Alakayleh, Xiaoning Li, Xueqian Li, Navid Jadidoleslam, Kyle Lusk.

I would like to give a special thanks to Jue Wang who always helped me to learn OpenFOAM and shared his knowledge about CFD modeling generously.

Due to the collaboration at the experiment, I would like to thank Merve Cetin.

I would like to thank all the people who have directly or indirectly helped me out in developing my research especially my sisters Safa Durmaz and Ozge Ozturk and my lovely brother Muhammet Eldayih and my friends from Turkey, including Deniz Kilic, Ebru Dinc, Hilal Ulkucan Tevetoglu, Elif Uyanik, Umit Demirbaga, Kubra Demirbaga, Ibrahim Gur, Hasan Alperen Turhan, Dilek Celebi.

Finally, I dedicate this degree to my father Ismail Eldayih and my mother Gulay Eldayih.

I would be lost, without your love and faith. I love you.

Table of Contents

List of Figures

List of Tables

List of Abbreviations

A	Pipe cross sectional area $= {}^{\pi}\!/_{4}\, D^2$
C_{air}	Celerity of the air $C_{air} = C_i\sqrt{gD}$
C_i	Correction factor that depends on the thickness at the downstream end
C_p	Specific heat
D	Pipe Diameter
f	Friction factor
F_I	Interfacial Froude number
F_c	Critical Froude number
$H*$	Normalized pressure Head ($H* = \frac{H}{D}$)
H_{water}	Hydraulic depth of water
H_{air}	Hydraulic depth of air
K	Loss due to the entrance and the discharge
K_f	Correction factor
L	Length of the rigid-column

P	Pressure
S_T	Energy source term,
S_U	Momentum source term
$T*$	Normalized Time ($T* = T*\frac{\sqrt{gD}}{L}$)
T	Temperature
t	Time
U	Velocity vector
U_r	Velocity field at the air-water interface
V_a	Bore velocity
$V*$	Normalized velocity ($V* = \frac{V}{\sqrt{gD}}$)
V_{FS}	Free surface velocity
Y_0	Water level at the upstream reservoir
Y_2	Water level at the downstream end of the pipe
α	Volume fraction of the liquid and gas in a cell ($0 < \alpha < 1$)
λ	Wave length of the water wave.
μ	Dynamic viscosity

ρ	Density
ρ_{water}	Density of water
ρ_{air}	Density of air

Chapter 1

1.Introduction

Stormwater drainage systems may experience unsteady inflows and hydraulic transients as the regime changes from free surface flow to pressurized flow during the intense rain events. Air phase that is initially present in systems is displaced by the water inflows. During the replacement of air by water, air pockets may appear within the pressurized flow regions. According to Vasconcelos and Wright (2006), there can be various mechanism leading to air pocket formation in a closed conduit system, and one of them is shear flow instabilities (SFI). Understanding the mechanism and kinematic conditions of air-pocket entrapment due to shear flow instabilities is important to prevent undesirable operational problems such as surging, structural damage, manhole cover displacement, and geysering events (Muller et al. 2017). Figure 1.1 shows separate manhole cover displacements and geysering events recorded during intense rain events.

Figure 1. 1: Different geysering events due to the intense rain (a) Minneapolis, MN on 10/05/2013 (b)Tualatin, OR on 9/22/2013

Since sewer and tunnel system are opened to atmosphere via manholes and shafts, stormwater systems are designed to operate in free surface flow regime. When entrapped pockets are formed, the motion of these resemble discrete gravity currents. One of the pioneer studies about the gravity current was presented by Benjamin (Benjamin, 1968), who studied the motion of an air cavity created by a sudden discharge in one end of a closed rectangular pipe. The leading edge of gravity currents or discrete air pockets moving in a pipe with diameter D has a celetrity value that scales with $\sqrt{gD}$ m with g being gravity acceleration. Benjamin pointed that the cavity celerity decreases as its thickness decreased.

Follow up investigations on gravity currents were presented by (Wilkinson, 1982) and (Baines 1991). According to Wilkinson, air-cavity cannot be in a steady-state unless the height of the water under the cavity is less than 0.78 of the pipe height. The situation of air-entrapment under atmospheric conditions was studied by Baines. In that study, increase at the weir height controlling the outflow, and the increase at the slope of the pipe was used to study changes in the celerity of air pockets' leading edge of an entrapped air in a pipe. More details in each of these studies are presented in Chapter 2.

As pointed by Li and McCorquodale (1999), air pocket formation based on shear flow instabilities occur when rapid air flows occur over water flowing in the free surface regime. At a certain relative air-water velocity threshold, water waves will grow and reach pipe crown, creating an entrapped air pocket. Arai and Yamamoto (2003) presented an interesting study on the limiting flow conditions that would result in SFI. In the first part of the study, Arai and Yamamoto (2003) studied the computational model and experiment. They have realized that the existence of the entrapped air in the system increases the maximum pressure, but experimental confirmation is still lacking. This is one of the main motivations for this study.

Since the focus of previous investigations in gravity current and cavity flow was not linked to the development of SFI, these works did not involve changes in flow conditions (i.e. unsteady flows) during the air cavity advance. As a result, apart from the Baines experiments who investigating gulping at the outlet location in pipes, there was no systematic investigation on air pocket formation in these contributions. To create conditions that would result in pocket formation via SFI, the strategy used in this investigation was to create air cavity flows and change in flow conditions that suddenly led to large relative velocity between air and water. Using experimental results and numerical results, this work considered various characteristics of this type of two-phase flows, including air pocket volumes, multiple pocket formation, as well a comparison between the pocket format observed in experiments and numerical predictions.

Chapter 2

2. Literature Review

This chapter presents the relevant literature review and is structured in four sections to cover the theoretical aspects that are relevant to this research, as follows:

- Gravity currents
- Shear flow instabilities
- Air pockets in stormwater systems
- Computational fluid dynamics

2.1 Gravity Currents

An air cavity occurs when the end of a water-filled pipe is opened suddenly allowing water to be freely released into the atmosphere. One of the early studies about the motion of the gravity current in a rectangular and circular pipes was done by Benjamin in 1968. Benjamin ignored the effects of viscosity and the interaction between two fluids at the interface. He assumed that horizontal momentum and hydrostatic forces are in a balance. Basically, Benjamin studied gravity currents which are in a steady-state condition. According to Benjamin's steady-state assumption, celerity of the cavity in a fully open horizontal circular pipe is $0.542(gD)^{1/2}$, where D is the diameter of the pipe that is shown at Figure 2.1 (Benjamin, 1968). In the Figure 2.1, O is the stagnation point, the pressure was admitted as zero through the free surface. When Bernoulli's theorem is applied with no energy loss assumption through the surfaces, Equation 2.1 was obtained by Benjamin. Likewise, conservation of mass equation is expressed in Equation 2.2.

:

$$C_2^2 = 2g(d - h) \tag{2.1}$$

$$C_1 * \mathrm{D} = C_2 * h \tag{2.2}$$

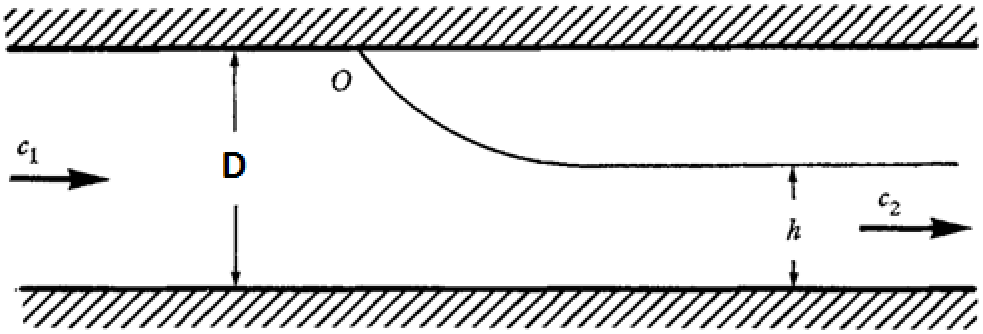

Figure 2. 1:Key variables in the steady flow past an air cavity (Benjamin, 1968).

Steady-state condition implies that pressure forces and momentum fluxes are in balance. For the upstream side of the pipe, total force is S_1 (Equation 2.3) and for the downstream side of the pipe total flow force is S_2 (Equation 2.4). In case of the assumption of $S_1 = S_2$ and with the combination of Equation 2.2, Equation 2.5 can be obtained.

$$S_1 = \frac{1}{2}\rho(C_1^2 D + gD^2) \tag{2.3}$$

$$S_2 = \rho(C_2^2 h + \frac{1}{2} gh^2) \tag{2.4}$$

$$C_2^2 = \frac{g(D^2 - h^2)D}{(2D - h)h} \tag{2.5}$$

Equation 2.5 indicates that when the cavity thickness decrease (i.e. h is increased), the celerity of the cavity will decrease. Figure 2.2 shows the relationship between cavity thickness and celerity which is at the maximum ($0.542(gD)^{1/2}$) in the case of a rectangular pipe. Townson (1991) presents results that indicate that when circular pipe geometry is considered the cavity speed did not change substantially, as indicated in Figure 2.3. In the graphs, U_0 corresponds to the term C_1 in Equation 2.1, d0 is the pipe diameter D, d_2 is the free surface flow thickness h. The terms E_J, E_C and E_S correspond to energy loss

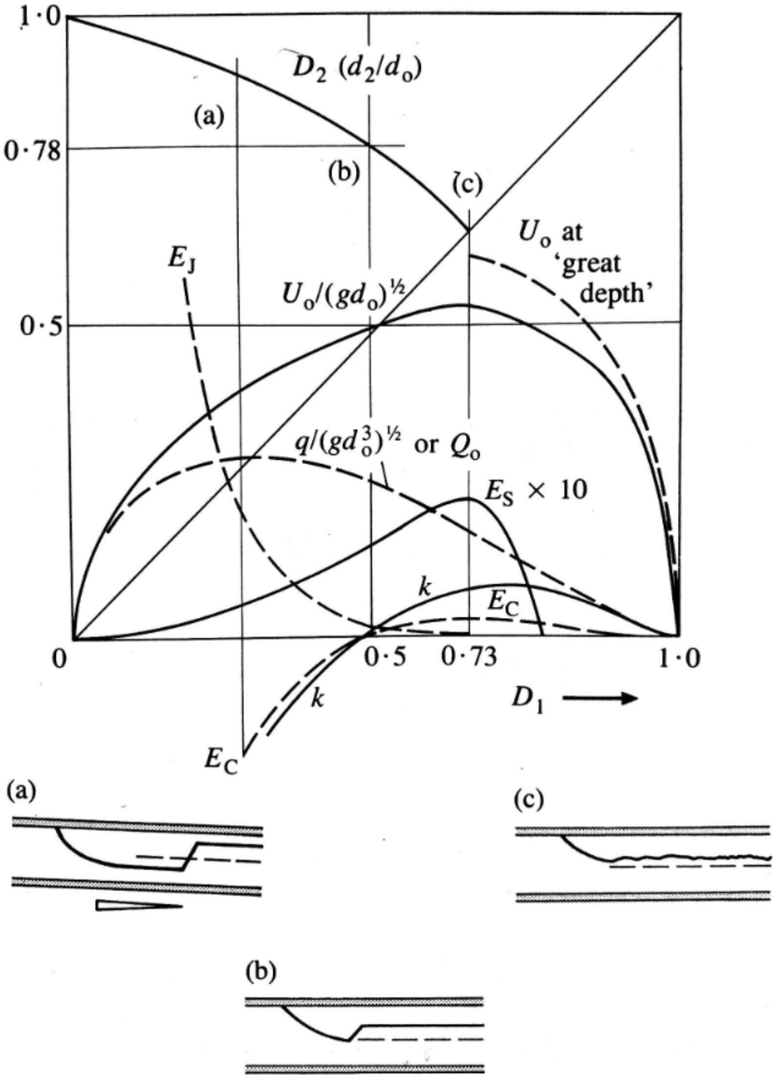

Figure 2. 2: Results from Benjamin’s theory supplemented with cases involving a hydraulic jump downstream. (a), (b) and (c) are located on the graph. (Townson,1991).

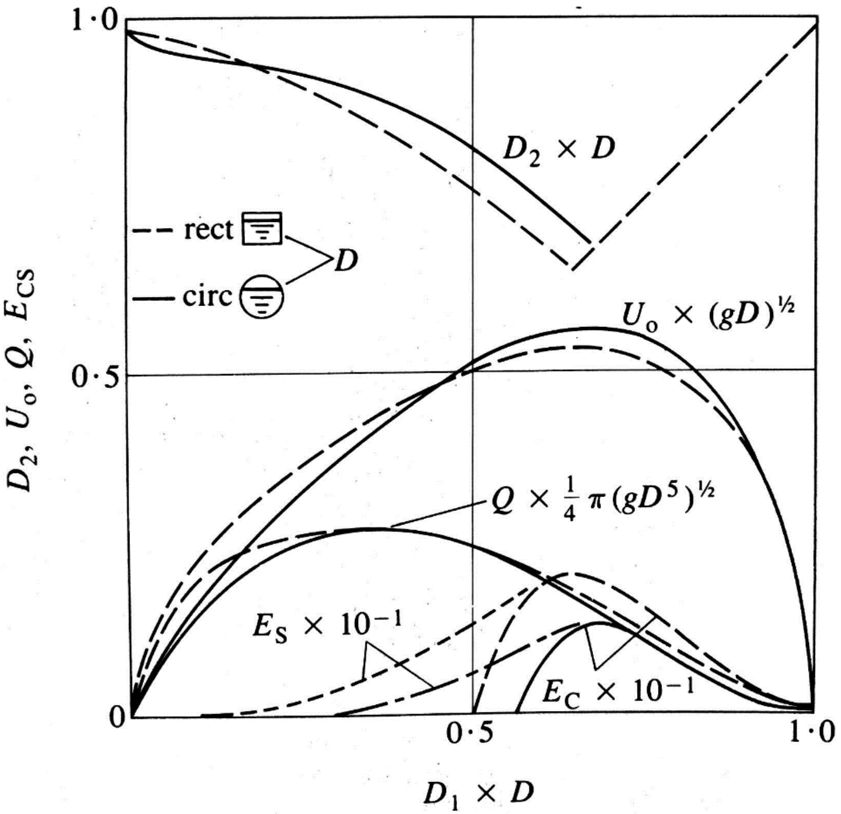

Figure 2. 3: Benjamin’s method applied to a circular section compared with the rectangular case (Townson,1991).

Benjamin also indicated that pressure is hydrostatic everywhere except from the region near the cavity itself, as is clear by the strong curvature of the cavity leading edge, as sketched in Figure 2.4. Due to the non-hydrostatic condition, one-dimensional mathematical models such as Saint-Venant Equation are not applicable, as they lack vertical acceleration terms, preventing an accurate representation of flows near cavities. This poses practical difficulties in modeling air-water flow conditions in closed conduits that have entrapped air pockets.

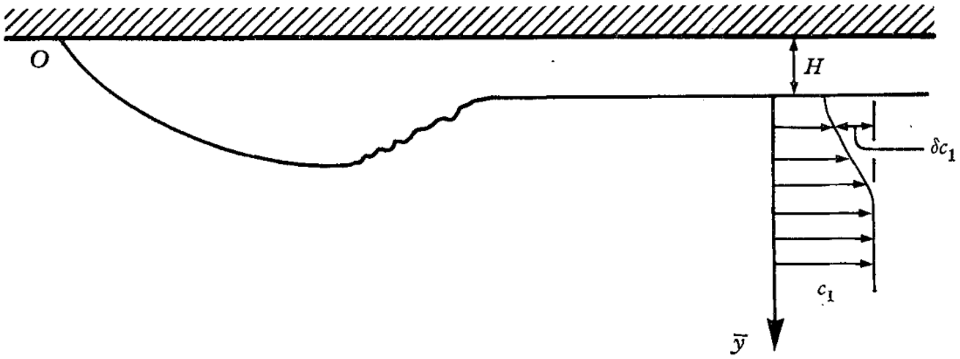

Figure 2. 4: Illustration of real flow, showing breaking head wave and velocity profile of ensuing wake (Benjamin, 1968).

Wilkinson expanded Benjamin work by studying the limitations of the steady-state condition of the cavity flow in 1982. According to Wilkinson, increasing the height of the weir causes an increase at the celerity of the bore so that the celerity of the leading edge and the celerity of the bore comes closer by the increase at the weir height. As a result, a steady-state condition occurs only if the water depth under the cavity is greater than 0.78 of the pipe height. Otherwise, the cavity divides into two uniform parallel flows with a bore region which are front and behind bore regions as is shown in Figure 2.2. Front region is speeder than the bore, thereby extended length of the front region. (Wilkinson, 1982).

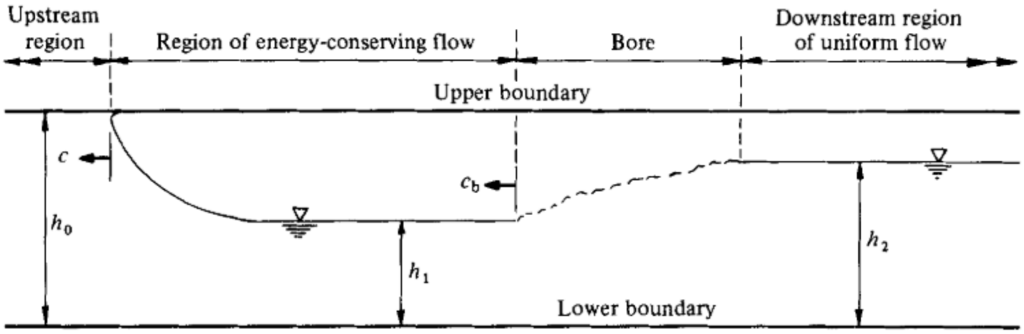

Figure 2. 5: Schematic diagram of the cavity flow in a closed conduit (Wilkinson, 1982).

Baines (1991) investigated the effects of the slope on the air cavity by applying the weir with the different heights at the outlet of the duct both experimentally and theoretically. Baines studied the motion of discrete air pockets, and the leading edge of these cavities had a celerity that was comparable to the cavities studied by Benjamin and Baines. He also observed air entrapment through gulping in the downstream end of the apparatus into the duct for two situations: (1) when the slope is 2^{o} and weir height at the outlet is equal to the 0.75 of the duct height (Figure 2.6); and (2) when the slope is 8^{o} and weir height is 0.5 of the duct height. This showes that the air entrapment occurs even if the pipe is nearly horizontal by installing weirs at the outlet of the duct.

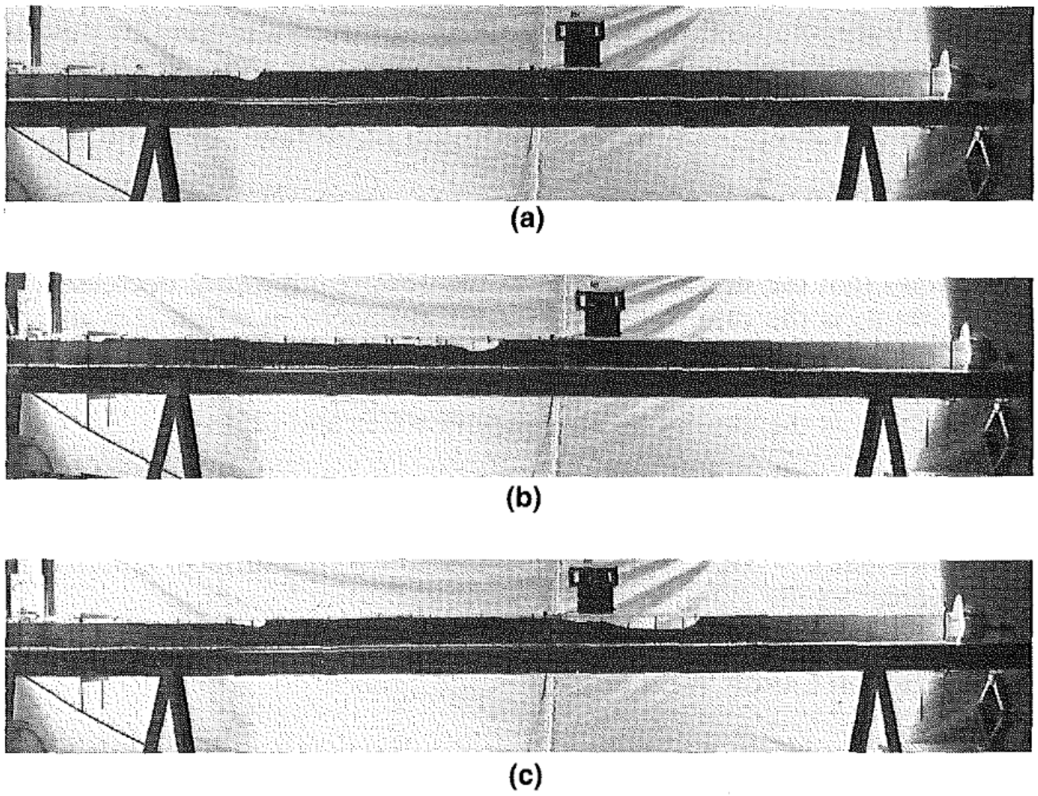

Figure 2. 6: Photos of Progression of Small Finite Cavity after Sealing. Experiment 091 with e = 2°, H = 0.75. (a) Cavity Is not Sealed and Has Long Tail with Horizontal Surface; (b) Cavity in Center Is Sealed, Tail Has Shortened, and Front is Larger; (c) Cavity at Right Shows Profile of Finite Volume Cavity, Tail is smaller (Baines 1991)

Chosie et al. (2014) worked on various factors that have effects on the celerity of the discrete gravity current's leading edge; such as air-pocket volume, background flow and slope. According to this study, thin air pockets cannot propagate for a long time when there is a background flow in a horizontal pipe. It starts to move backward because of the shear stress and adverse flow, as is shown in Figure 2.7, but soon shearing stops this pocket propagation.

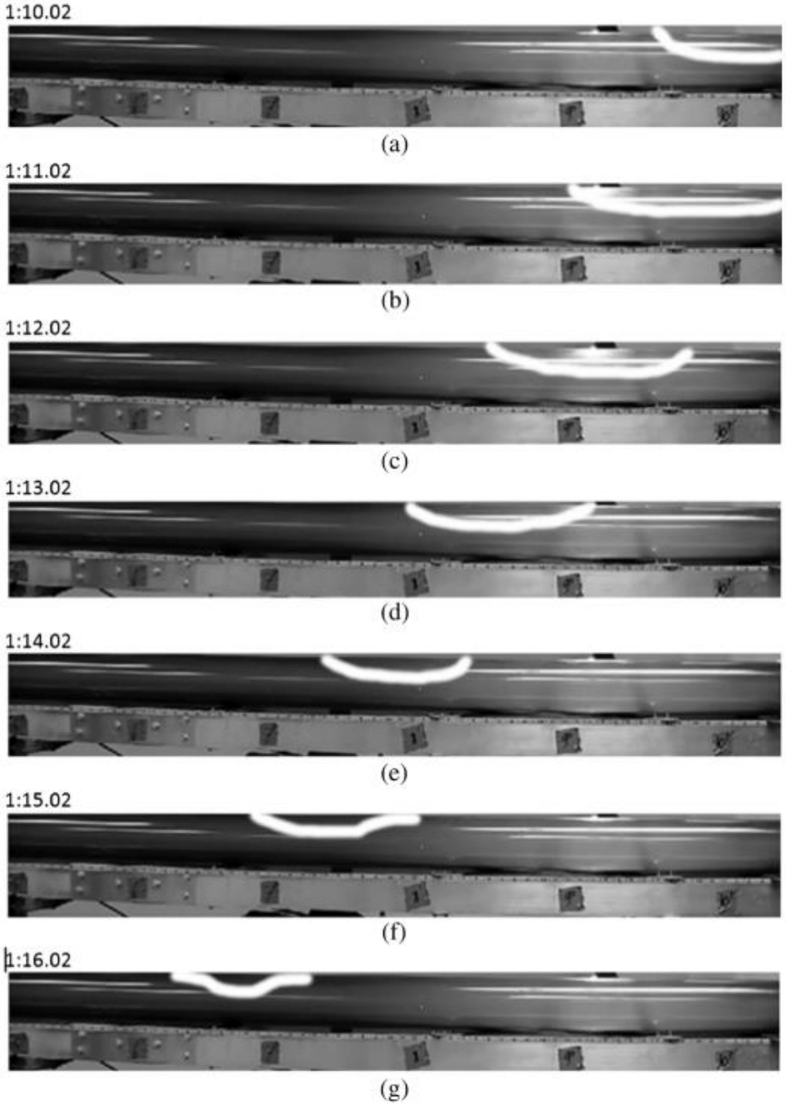

(a)
(b)
(c)
(d)
(e)
(f)
(g)

Figure 2. 7: Sequence of snapshots illustrating the trajectory of the horizontal slope, illustrating the shearing process; the interface between backward-moving pocket trajectory for air/water interface is enhanced (Chosie et al. 2014)

One limitation of many of these studies is that there is no flow velocity into the duct. However, in real applications, there is often some flow inside closed conduits. The sudden change in the pressure causes broken pumps, valves and pipes, and operational problems into the water systems. It frequently occurs due to the flow regime transition from free surface flow to the pressurized flow and produces uncontrolled air release.

2.2. Shear flow instabilities

The mechanism of parallel flows studied by Reynolds in 1983. He tried to find out a physical description of the mechanism of instability by using viscous and inviscid flows. Figure 2.8 shows the laminar, turbulent flows, and eddies in a turbulent flow. This was the first experiment and observation of the flow instability created by turbulence.

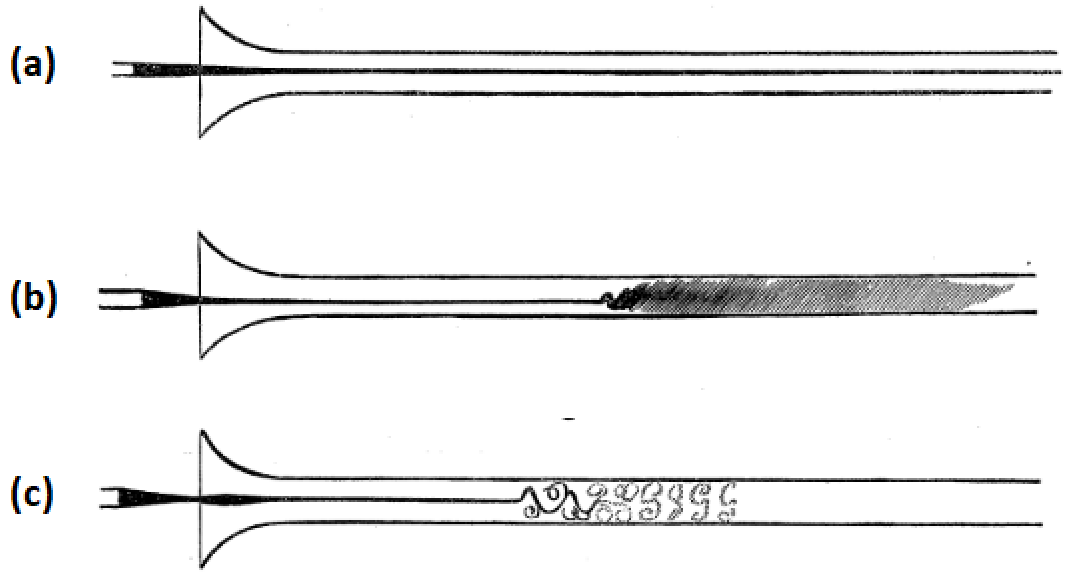

Figure 2. 8: (a) Laminar flow (b)Turbulent Flow (c)Turbulent flow when it observed with an electric spark. (Reynolds, 1883)

Other researchers in the 19th century also studied instability in flows, such as Helmholtz in 1868 and Kelvin in 1871. (Batchelor, 1967) explained the physical mechanism of Kelvin-

Helmholtz instabilities in terms of regards vorticity dynamics as is shown in Figure 2.9. The local strength of the sheet is represented by the thickness of the sheet. The arrows indicate the directions of the self-induced movement of the vorticity in the sheet, and show (a) the accumulation of vorticity at points like A and (b) the general rotation about points like A, which together lead to exponential growth of the disturbance.

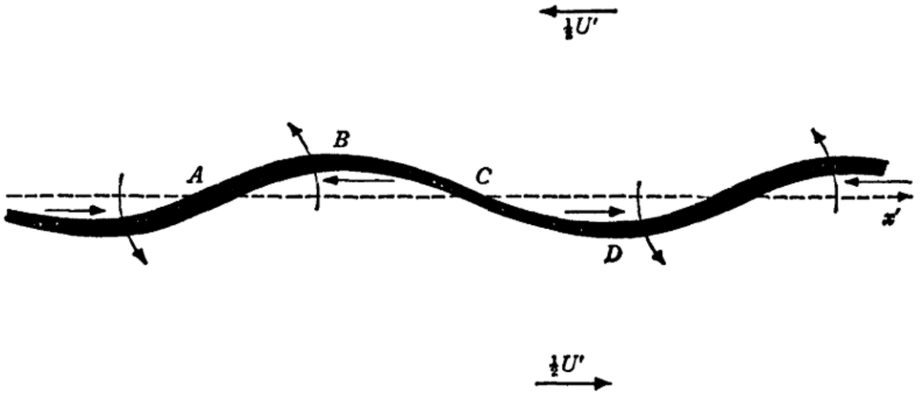

Figure 2. 9: Growth of a sinusoidal disturbance of a vortex sheet with positive vorticity normal to the paper (Batchelor, 1967).

An mechanism analogous to Kevin-Helmholts instabilities, referred to as shear flow instabilities (SFI), was described by Hamam and McCorquodale in 1982 as a process that creates interfacial disturbances until it creates air-pocket entrapments through the surface (Hamam & McCorquodale, 1982). It occurs when the velocity at the air-water interface is in the opposite direction and the same magnitude. (Baines and Mitsudera, 1994). The study of Hamam and McCorquodale in 1982 was advanced by Li and McCorquodale (1999) to develop a criterion for interfacial instability (which will be further explained in Chapter 4) that is due to the transition from free-surface flow to pressurized flow. The stages of transition from free surface flow to pressurized flow is shown in Figure 2.10. According to this study, instability depends on pipe diameter, flow velocity, entrance and discharge condition, pipe length, pipe shape, wave height, and flow height in the pipe (Li and McCorquodale 1999).

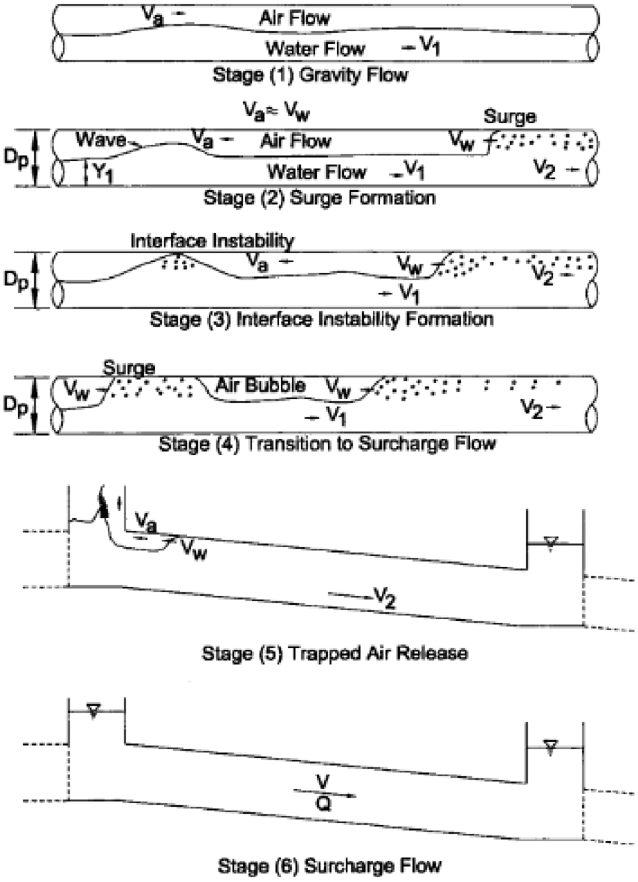

Figure 2. 10: Stages in Transition of Free-Surface to Pressurized Flow (Li & McCorquadale, 1999)

Kordyban presented different criteria for the shear flow instabilities that also depended on the maximum air velocity at the inside of the conduits in 1999. According to this study, expressions to evaluate the threshold of Kelvin-Helmholtz instabilities can be divided into four groups. The first group assessed SFI regarding wave motion equations and over-estimates the gas velocity. The second group ignores wave motion but focuses on the slug formation and uses the Bernoulli Equation to analyze instability. This group over-estimates gas velocity as well. The third group evaluates instability by considering energy flux. However, while the results are good matches with their data, they were not matched well with the other researchers' studies. The fourth group of researchers considers inertia and friction's effects to understand instability and were obtained in an up-and-coming agreement in this area (Kordyban, 1990). These mathematical models were used to verify our CFD model. Another work that accounted for SFI was presented by (Arai and Yamamoto 2003), who created a two-phase mathematical model to simulate rapid filling, assuming that a relative air-water velocity threshold would lead to air pocket entrapment .

An experimental study for the investigation of various air pocket entrapment mechanisms, including SFI, was presented by Vasconcelos and Wright in 2006. Three ventilation towers were installed through the pipe. SFI, air-pocket entrapment and geysering events were investigated by changing the location of ventilation towers and the inflow rate. As a result of this study, researchers deduced that air-pocket entrapments can cause by misplaced or inadequate ventilation tower, breakdown at the air-water interface or due to the shear flow instabilities. All the possibilities shown in Figure 2.11, 2.12, 2.13, and 2.14.

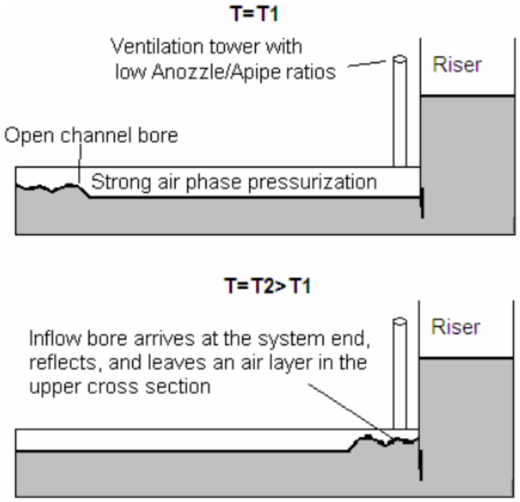

Figure 2. 11: Illustration of the VENT mechanism for air pocket entrapment - Inadequate amount of ventilation (Vasconcelos and Wright 2006).

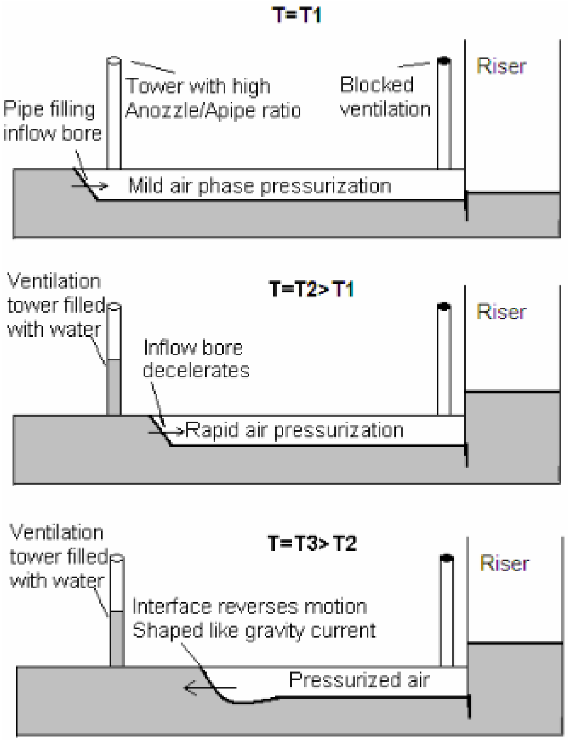

Figure 2. 12: Illustration of the GEO mechanism for air pocket entrapment - Geometrically misplaced ventilation (Vasconcelos and Wright 2006).

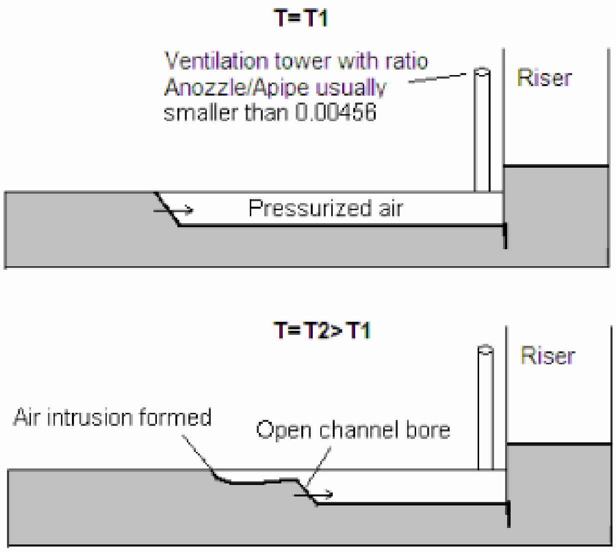

Figure 2. 13: Illustration of the IBD mechanism for air pocket entrapment - Interface Breakdown (Vasconcelos and Wright 2006).

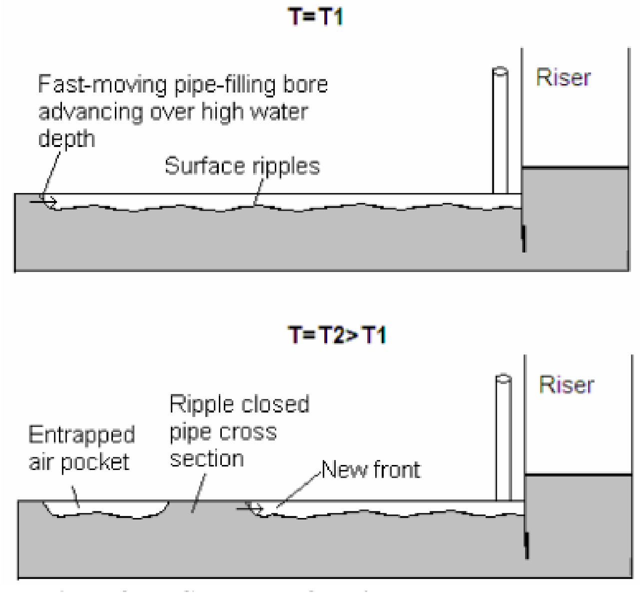

Figure 2. 14: Illustration of the SFI mechanism for air pocket entrapment - Shear flow instability (Vasconcelos and Wright 2006).

2.3 Air pockets in stormwater systems

During extreme inflow conditions, stormwater systems may experience unsteady inflows and the transition between free surface and pressurized flow regimes. The probability of having transition to the pressurized flow in the pipe is very high when the water depth is higher than 0.85 of the pipe diameter or fraction of the air in the pipe is around 0.1 (Hamam & McCorquodale, 1982). Air phase that is initially present in systems can be dislodged by water inflows, and during the filling stages, air pockets may appear within the pressurized flow regions. As Vasconcelos and Wright (2006) showed, there are various air pocket entrapment mechanism. Entrapped air pockets have been linked to various operational problems in storm water systems, including surging, structural damage, manhole cover displacement, and geysering events (Muller et al. 2017).

An experimental study by Vasconcelos and Wright (2008) evaluated the advance of an air cavity into a water-filled circular pipe in horizontal slope upon the sudden opening of a downstream end. Because the upstream end of the apparatus was fitted with an air reservoir the advance of the air cavity was sometimes halted and reversed as the water column in the horizontal pipe gained velocity. In other cases, there was not enough pressure to eliminate air in the system, and the flow evolved from a curved gravity current into a H2 gradually varied flow profile within a pipe due to the critical discharge conditions at the outlet. A modification of this experimental apparatus is used in the present research.

Rapid filling and emptying of the pipe was studies in a large experimental apparatus by Laanearu and collaborators. According to this study, in addition to the shear at the pipe walls, there is another shear between air and water that causes by the intrusion of the air into the pipe. The instability is associated with this additional shear. Also, they found that the air-cavity celerity is larger when the pipe is emptying than filling. This is apparently because of the length of the water column which is the whole pipe at the beginning of the emptying pipe Laanearu et al. (2016).

Another study based on the kinematics of emptying a horizontal circular pipe was done by Bashiri-Atrabi et al. (2016). The authors stated that long, horizontal pipe flow can be divided into three types: steady, unsteady, and steady dissipative regime flow depending on the height of the weir at the downstream. There was no weir used to create a steady flow, the weir height was 50% of the diameter to create an unsteady flow, and it was 0.7 of the diameter to create a steady dissipative regime flow. The weirs also were used to create an undular bore, and the study was about the comparison of the numerical models that were based on the hydrostatic assumption and Boussinesq equation. Consequently, as is shown in the Figure 2.15, they found that the Boussinesq model was better than the Saint Venant (i.e. hydrostatic) model to determine cavity shape and position, and water surface profile. (Bashiri-Atrabi et al., 2016).

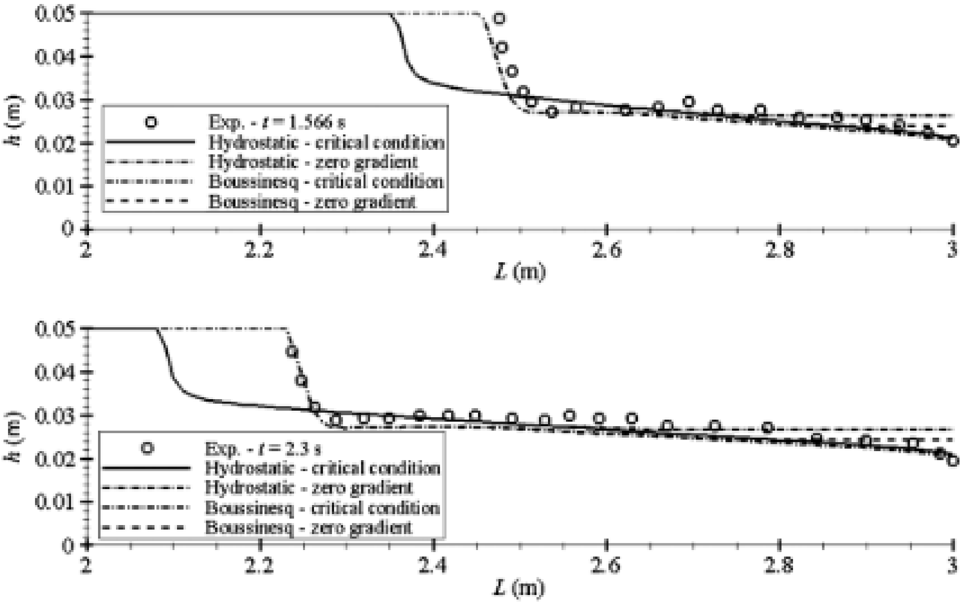

Figure 2. 15: Simulation of cavity surface profile and end depth using hydro-static and Boussinesq models ($h_w = 0.0$, $\theta = 0°$) (Bashiri-atrabi et al., 2016)

Air pocket entrapment due to the air-water interaction has been studied by Chosie et al. (2014), and the celerity of the entrapped air-pocket has been determined and kinematic of the air pocket investigated. According to this study, air pocket velocity is related to the slope of the pipe when the volume of the air pocket is small (Figure 2.16). However, when the air pocket volume is larger and the leading edge is thicker, it is not affected by the slope of the pipe (Figure 2.17).

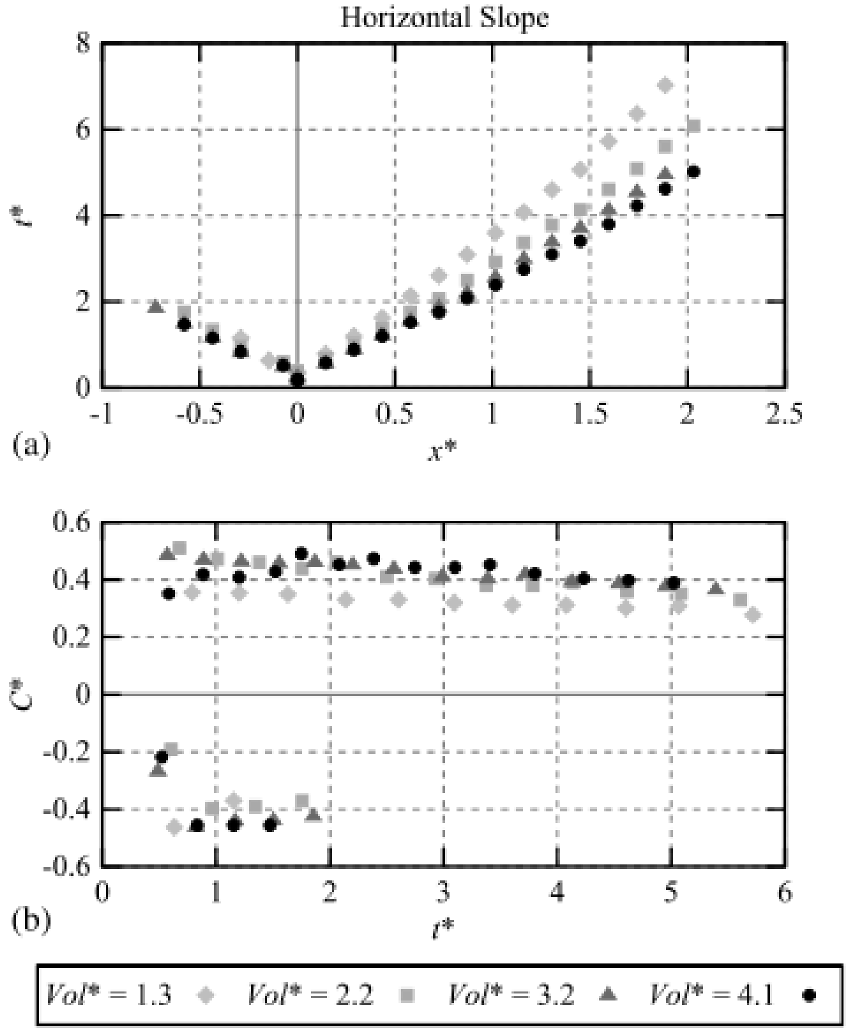

Figure 2. 16: Trajectory of the air pocket leading edge and observed celerity for horizontal slope and various air pocket volumes and no pipe flow; negative coordinates indicate pockets are propagating toward upstream Chosie et al. (2014).

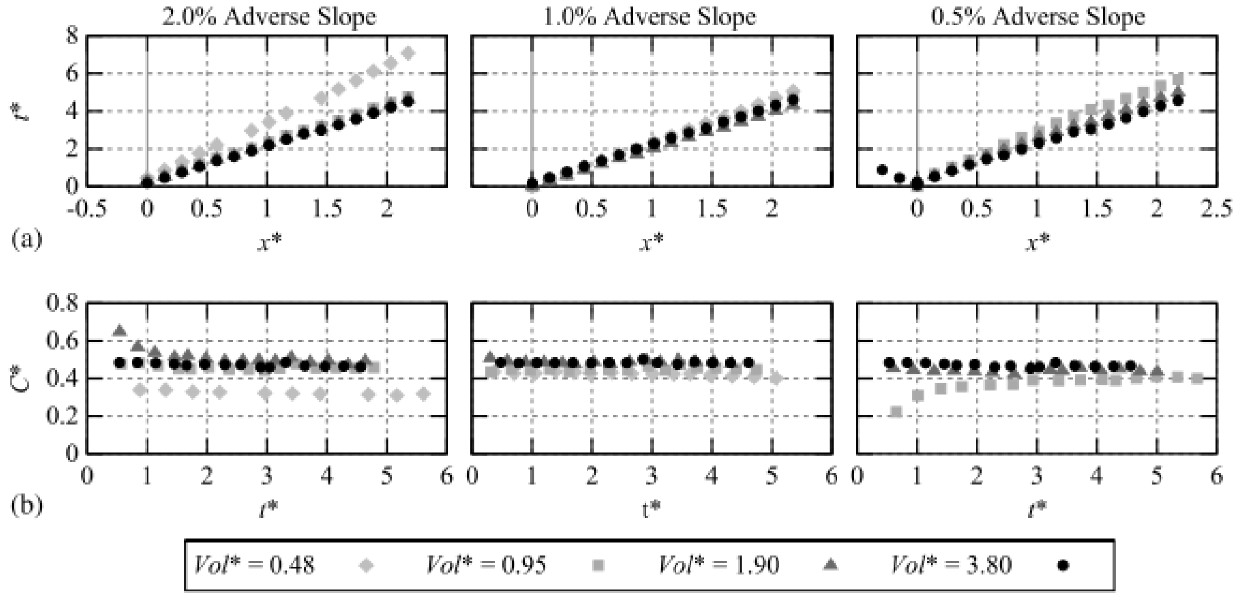

Figure 2. 17: Trajectory of the air pocket leading edge and observed celerity for various adverse slopes and air pocket volumes and no pipe flows; negative coordinates indicate pockets are propagating toward upstream (Chosie et al. 2014).

2.4. Computational fluid dynamics

The combination of mass conservation and a linear momentum conservation in three dimensions (3-D) yield a system of partial differential equations referred to as Navier-Stokes (NS) equations. (Equation 2.6, 2.7,2.8 and 2.9), which enable description of complex fluid flows:

$$\frac{\partial \rho}{\partial t}+\frac{\partial \rho u}{\partial x}+\frac{\partial \rho v}{\partial y}+\frac{\partial \rho w}{\partial z}=0 \tag{2.6}$$

$$\rho\left(\frac{\partial u}{\partial t}+u\frac{\partial u}{\partial x}+v\frac{\partial u}{\partial y}+w\frac{\partial u}{\partial z}\right)=-\frac{\partial p}{\partial x}+\mu\left(\frac{\partial^2 u}{\partial x^2}+\frac{\partial^2 u}{\partial y^2}+\frac{\partial^2 u}{\partial z^2}\right) \tag{2.7}$$

$$\rho\left(\frac{\partial v}{\partial t}+u\frac{\partial v}{\partial x}+v\frac{\partial v}{\partial y}+w\frac{\partial v}{\partial z}\right)=-\frac{\partial p}{\partial y}+\mu\left(\frac{\partial^2 v}{\partial x^2}+\frac{\partial^2 v}{\partial y^2}+\frac{\partial^2 v}{\partial z^2}\right) \tag{2.8}$$

$$\rho\left(\frac{\partial w}{\partial t}+u\frac{\partial w}{\partial x}+v\frac{\partial w}{\partial y}+w\frac{\partial w}{\partial z}\right)=-\frac{\partial p}{\partial z}+\mu\left(\frac{\partial^2 w}{\partial x^2}+\frac{\partial^2 w}{\partial y^2}+\frac{\partial^2 w}{\partial z^2}\right)+\rho g \tag{2.9}$$

Where ρ is the fluid density, u, v, w are the velocity components in the Cartesian x, y and z axis, p is the local pressure, μ is the dynamic viscosity, and g is gravity acceleration.

Navier-Stokes equations are too complex to be solved analytically without introducing a large number of simplifications. Therefore, numerical solution is needed when unsteady two-phase flow applications are considered, which is often achieved with the use of Computational fluid dynamic (CFD) approach. This involves solving NS numerically through discretization, adopting a numerical method and numerical schemes to solve for the flow in time and space. In this process, turbulence will be an integral part given the large Reynolds number of such flows. Direct solution of turbulence is difficult because of the small discretization needed to resolve the smallest turbulent eddies. Thus turbulence modeling was adopted in this research, and the standard *k*- ε turbulent model (Equations 2.10 and 2.11), as used by Matsubara et al. (2013), was selected to represent turbulence in cavity flows.

$$\frac{\partial(\rho k)}{\partial t} + \nabla(\rho U k) = \nabla\left(\left(\mu + \frac{\mu t}{\sigma k}\right) + \nabla k\right) + P_K + P_{KB}\varepsilon - \rho\varepsilon \tag{2.10}$$

$$\frac{\partial(\rho \varepsilon)}{\partial t} + \nabla(\rho U \varepsilon) = \nabla\left(\left(\mu + \frac{\mu t}{\sigma_\varepsilon}\right) + \nabla \varepsilon\right) + \frac{\varepsilon}{k}\left(C_{\varepsilon 1}(P_K + P_{\varepsilon b}) - C_{\varepsilon 2}\rho\varepsilon\right) \tag{2.11}$$

Where *k* is, turbulence kinetic energy, ε is turbulence dissipation, P_{KB} and $P_{\varepsilon b}$ are the influence of buoyancy forces, P_K is turbulence production due to the viscous forces, $C_{\varepsilon 1}$=1.44, $C_{\varepsilon 2}$=1.92, σk=1, and σ_ε=1.3 are constant values.

CFD modeling of Navier-Stokes equations was implemented through OpenFOAM, which is an open source C++ toolbox that can perform both single-phase and multi-phase flows. Two-phase flow modeling was performed using the Volume of Fluid (VOF) method to track air-water interfaces (Hirt and Nichols, 1981). OpenFOAM has several flow solvers, and in this study compressibleInterFoam solver was selected to simulate non-isothermal, immiscible flows considering compression of air. Governing equations to represent this two-phase flow conditions, including continuity, momentum, and energy are presented in Equations 2.12, 2.13, and 2.14 below, respectively. Equation 2.15 is associated with the compression effects on the air-water interface.

$$\frac{\partial \rho}{\partial t} + \nabla \cdot (\rho U) = 0 \tag{2.12}$$

$$\frac{\partial (\rho U)}{\partial t} + \nabla \cdot (\rho U U) = -\nabla p + \nabla \cdot (\mu \nabla U) + S_U \tag{2.13}$$

$$\frac{\partial (\rho C_p T)}{\partial t} + \nabla \cdot \left(\rho U C_p T\right) = \nabla \cdot (k \nabla T) + S_T \tag{2.14}$$

$$\frac{\partial \alpha}{\partial t} + \nabla \cdot (\alpha U) + \nabla \cdot ((1-\alpha) \cdot \alpha \cdot U_r) = 0 \tag{2.15}$$

where U is the velocity vector, p is the pressure, μ is the dynamic viscosity, S_U is the momentum source term, C_p is the specific heat, T is the temperature, S_T is the energy source term, α is the volume fraction ($0 < \alpha < 1$), and U_r is the velocity field to compress the interface. The values of the α show the fraction of the liquid and gas volume in a cell (Svenungsson, 2016).

2.5 Summary and Knowledge Gaps

In summary, transient flow regimes can cause severe damage to urban water systems, particularly if two-phase flow conditions exist. Therefore, understanding air-water interactions created by the development of air pockets is an important issue to be investigated. In this context, studying the development of cavity flows, pocket formation due to shear flow instabilities become the main task of this study, given that much is not understood on the characteristics of SFI in closed conduits. While much was learned about the nature of cavity flows and discrete air pocket motion, previous studies did not attempt to determine how cavity flows evolve in bores, or what the entrapped air pocket volumes associated with SFI are. While many experimental studies on the topic where performed, much less focus was placed in using CFD to study SFI. These are the topics that motivated this research, as is discussed in the next chapter.

Chapter 3

3.Objectives

The present study focuses on the mechanism of shear flow instabilities to the development of air pockets in closed conduits undergoing rapid filling. It is the goal to determine the ability of CFD models to represent episodes of shear flow instability that were created in laboratory experiments. Experimental variables included the thicknesses of the air cavity that represented an initially stratified flow, and the rate of pipe filling through various pressures used in the reservoir that filled the pipe after the cavity advanced in the pipeline. Specific objectives of the study can be summarized as follows:

- To achieve a better understanding of the pocket formation in closed conduits created by air-water shear flow instabilities on the basis of previous studies.
- To collect experimental data for conditions involving SFI pocket formation for various air-phase geometries.
- To create and calibrate CFD model for all experimental tests to assess the accuracy of the model description of air pocket formation via SFI.
- To evaluate SFI threshold expressions based on the studies by Li and McCorquadale (1999).

Chapter 4

4.Methodology

This section presents details on the development of the experimental and numerical work associated with the research. Results are presented in non-dimensional fashion and normalized variables are marked with a star. Velocity and celerity values were normalized by $\sqrt{gD}$, time is normalized by $\sqrt{gD}/L$, and pressure heads were normalized by D, with D and L as the pipe diameter and length respectively.

4.1. Experimental Methods

The experimental investigation presented in this thesis is the current research focus by another MS student at the Civil Engineering Department (Merve Cetin). The results that are presented here are a summary of this work and resulted from a collaboration between Merve Cetin and this author.

4.1.1 Experimental apparatus description

Figure 4.1 presents the apparatus that consists in a 9.144-m long horizontal slope pipe with a diameter of 0.1016-m. The pipe is composed of three 3.048-m long pipes positioned in horizontal slope and joined with flexible pipe connectors. An upstream reservoir was filled with water with pressure head values of 0.305-m (1 ft), 0.610-m (2 ft) and 0.914-m (3 ft) above the pipe invert. The upstream reservoir was connected with a 0.102-m knife-gate valve that when was opened it supplied pressurized water into the pipe upstream end. A downstream reservoir was used to collect discharged water from the pipe. Another 0.102-m diameter knife gate valve was placed at the downstream opening of the horizontal pipe. At the downstream end, four different discharge conditions were considered: fully opened, and three weirs that blocked water flow partially, creating a gap near the pipe crown of 38,27, and 20mm (Figure 4.2). In total, 12 different experimental conditions were tested, and repeated 3 times to ensure consistency of results.

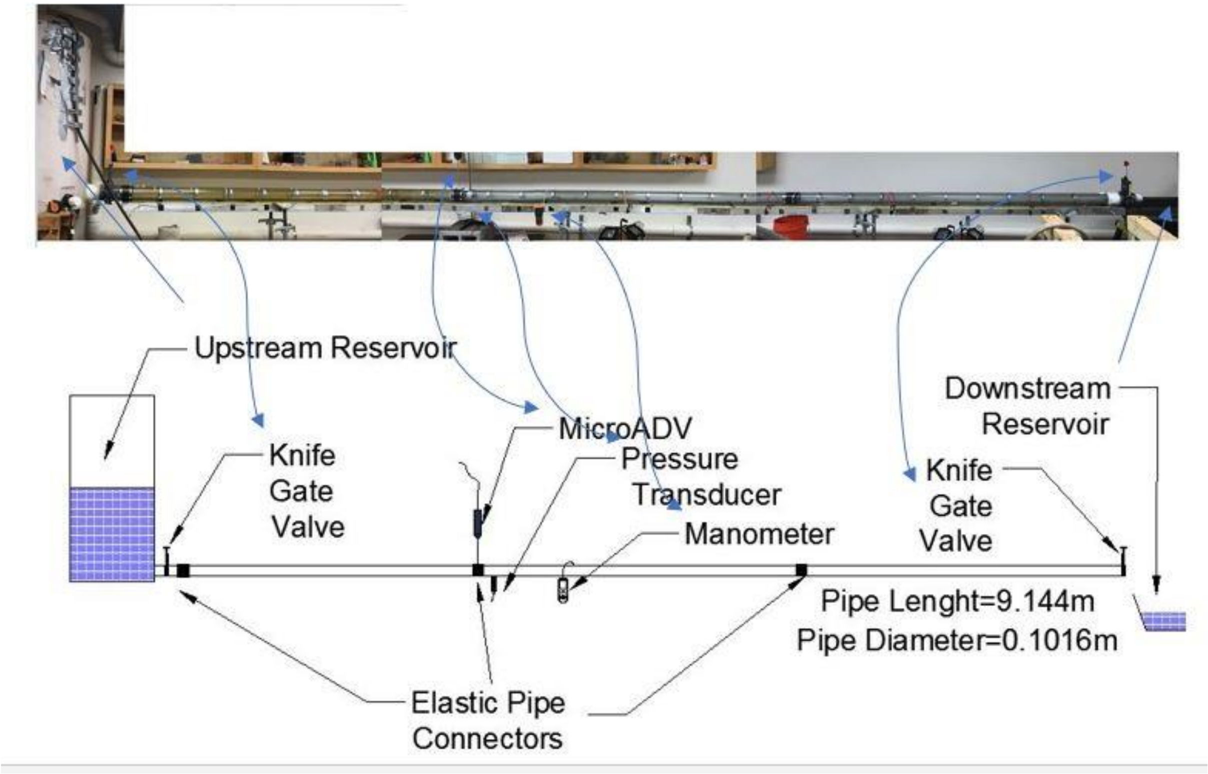

Figure 4. 1: Picture and sketch of experimental apparatus

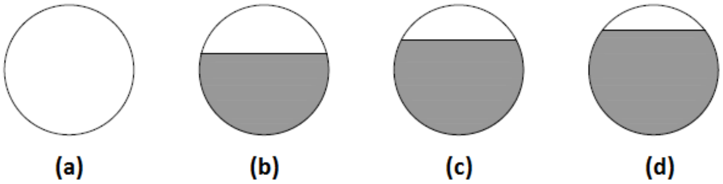

Figure 4. 2: Schematics of discharge conditions at the downstream end (a)Fully open pipe; (b) 38mm opening weir; (c)27mm opening weir; (d)20mm opening weir.

The instruments that were used in the experimental tests are listed below:

- Piezo-resistive pressure transducers: Transducer P1 (ENDEVCO 8510C-50) to record the pressure during the experiment was installed 3.18-m from the upstream end of the apparatus. It measures pressure up to 35-m head (Figure 4.3).

(a) **(b)**

r

Figure 4. 3: (a) Piezo-resistive pressure transducer (b) installation of piezo-resistive pressure transducer to the bottom of the pipe in the experiment.

- Manometer (EXTECH HD750, 5 PSIg): measured initial and final pressure of the horizontal pipe for each case, installed approximately 3.85-m away from the upstream valve. It can measure pressure up to 3.5-m head (Figure 4.4).

Figure 4. 4: Installation of manometer from the top of the pipe during the experiment.

- Velocity meter: MicroADV NORTEK was installed 3.048-m from the upstream valve to record the velocity. The frequency of data collection was 25 Hz (Figure 4.5).

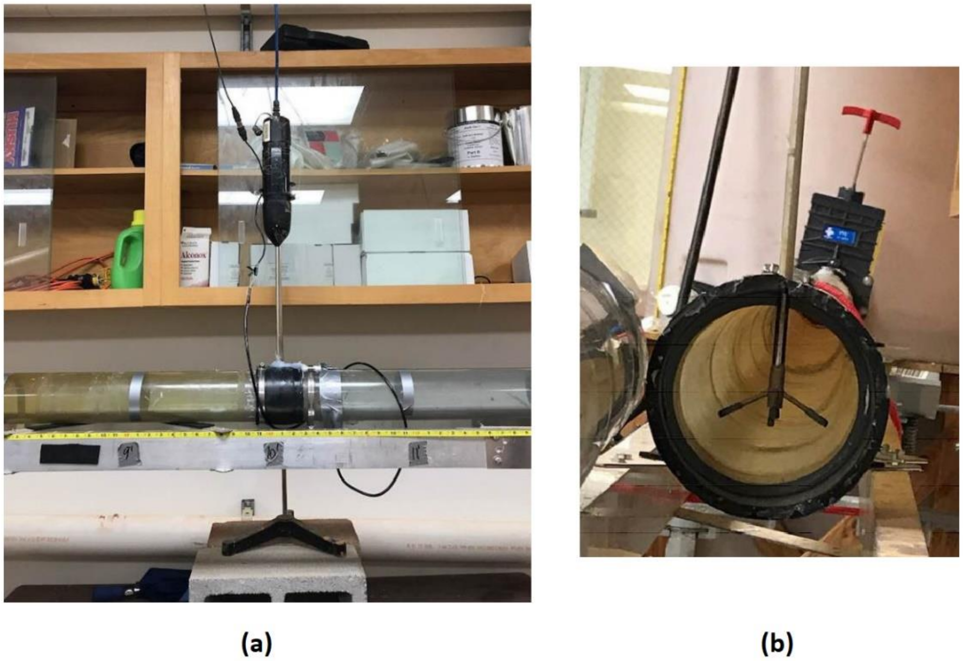

Figure 4. 5: (a) View of the ADV from the outside of the pipe. (b) View of the ADV from the inside of the pipe

- Data acquisition board: National Instrument NI-USB 6210 recorded the pressure transducer signals during the experiment (Figure 4.6) at a frequency of 200 Hz.

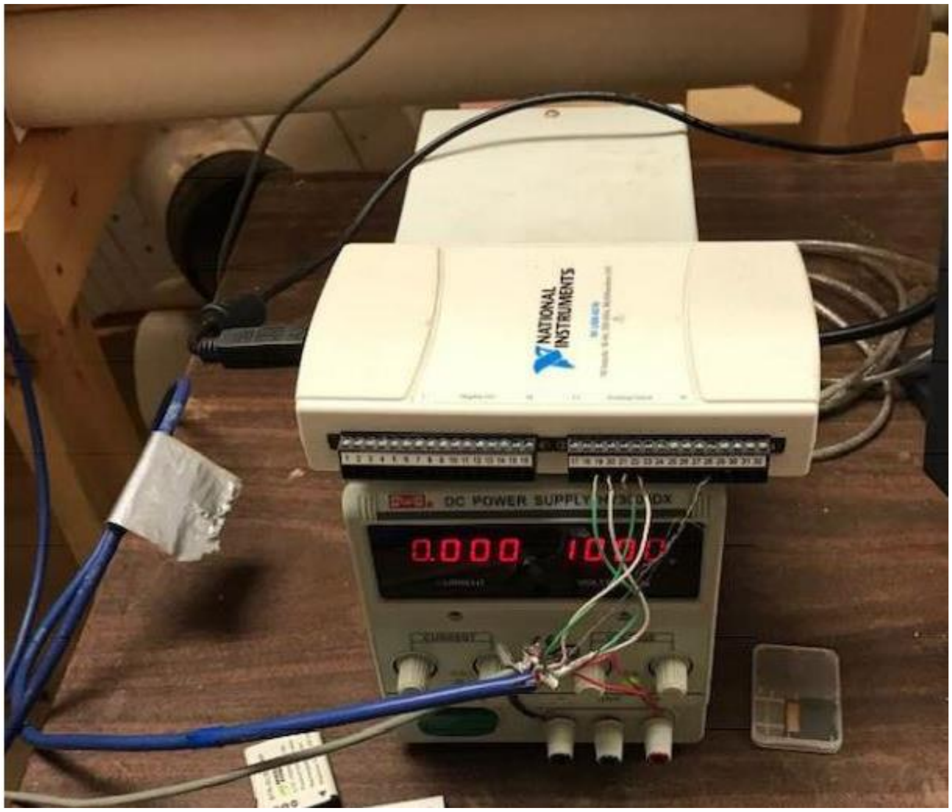

Figure 4. 6: Data acquisition board and its power supply.

- Three digital HD camcorders: recorded the overall experiment at 1080p resolution, 30 frames per second, recording flow profiles in each of the three pipes (Figure 4.7).

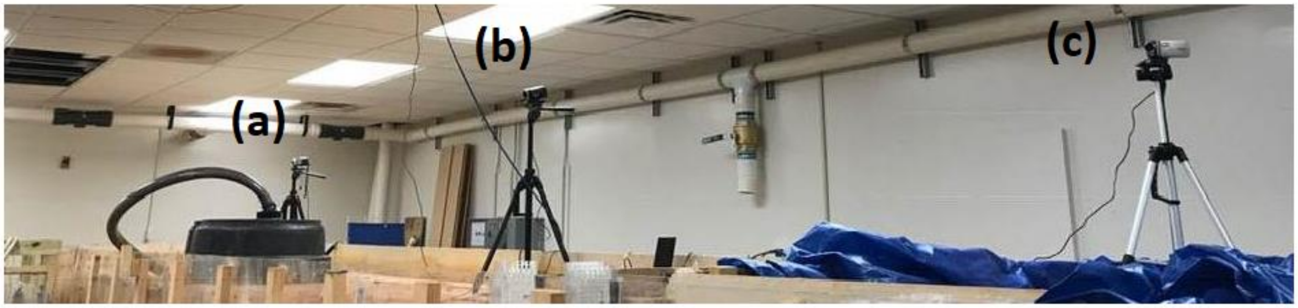

Figure 4. 7: Location of (a) Camera 1 (b) Camera 2 (c) Camera 3 used in the experiments.

- Supply reservoir: was installed to the upstream opening of the pipe. The water capacity of the reservoir was around 2.2m^3 (Figure 4.8), and it was used to provide the needed pressure at the upstream end of the pipeline after the nearby knife gate valve was opened.

Figure 4. 8: The reservoir at the upstream of the pipe, with the 102-mm knife gate valve installed at the base of the reservoir.

- Pipe junctions: Two 102-mm rubber pipe connectors were used to connect the three 3.05-m long pipe reaches (Figure 4.9). In one of these the MicroADV was also present.

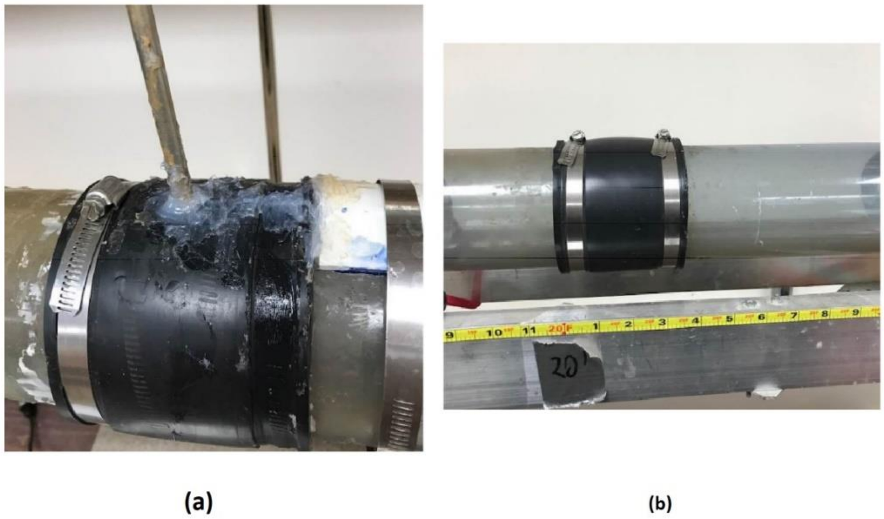

(a) (b)

Figure 4. 9: (a) The connection between first and second pipes. The ADV was applied to this location (10 feet from upstream) (b) The connection between second and third pipes (20 feet from upstream).

- Knife gate valve: Two 102-mm PVC knife gate valves were used. Upstream knife gate valve was used to control inflow and downstream knife gate valve was used to control outflow from the pipe (Figure 4.10).

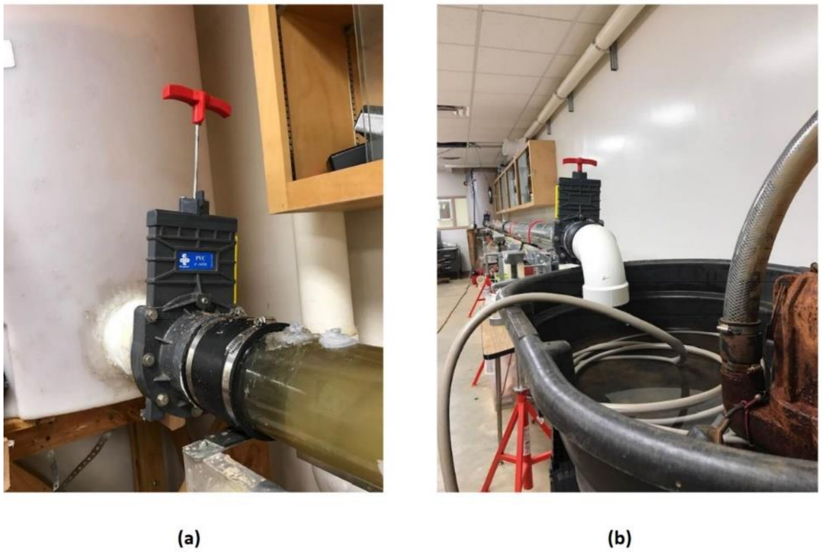

(a) (b)

Figure 4. 10: (a) The upstream knife gate valve (b) The downstream knife gate valve

4.1.2 Experiment description and experimental procedure

Initially the pipe was completely filled with water and no air existed in the whole apparatus. The experiment procedure then was initiated, and it consisted of two stages. In the first stage, a cavity flow was created by quickly (~0.3 to 0.5 second) opening the downstream valve to atmospheric air, resulting in water discharge at the downstream end. When a given weir was installed at the downstream end, the thickness of the air cavity decreased upon the opening of the downstream knife gate valve; the smallest thickness of the air pockets was yielded for the weir that created a 20-mm gap. The advance of the air cavity was consistent with the observations by Benjamin (1968) and others.

The second stage of the experiment was started when the air cavity approached the upstream end of the apparatus. At that point, the upstream valve linking the reservoir and the pipeline was quickly opened, which triggered the advance of water inflow from the reservoir in the upstream end. This inflow front created a pressurization condition that reversed the advance of the air cavity in the system and pushed the air out toward the downstream end. Depending on the pressurization level of the reservoir and on the thickness of the air cavity, the removal of the air phase in the system could be characterized in two possible outcomes: 1) a pressurized bore (i.e. flow regime transition pressurization interface); or 2) the formation of discrete entrapped air pockets due to shear force instabilities, which were ventilated at the downstream end.

The detailed procedure used in the experiments is presented below:

1. The downstream end of the pipe was prepared with an open condition (no weir) or with the positioning of a weir for partially opened cases.
2. The reservoir at the upstream was filled with water at the pre-specified height.

3. The apparatus was filled with water, and the bubbles were swept away from the pipe. Initially, both valves were closed, so water was in quiescent conditions.
4. Three HD camcorders were turned on.
5. Piezo-resistive transducer and velocity-meter ADV were started. The initial pressure was read and recorded from the manometer.
6. The knife gate valve at the downstream end was opened quickly (less than 0.5 second), and an air cavity propagated upstream near the pipe crown.
7. Shortly after the cavity reached the third pipe, the upstream knife gate valve was opened suddenly. Since the pressure was increased rapidly, the cavity was pushed by the advancing bore through the pipe.
8. The bore swept from the downstream end, and the knife gate valve at the downstream end was closed. The final pressure was read and recorded from the manometer.
9. The MicroADV, pressure transducers, and video cameras were turned off.

4.2. Computational Methods

The purpose of the numerical study is to create a computational fluid dynamics model (CFD model) for the cavity movement and air pocket entrapment due to the share flow instabilities. The geometries and meshes for each case have been created based on the experimental apparatus. Then, the CFD model was developed in the OpenFOAM.

OpenFOAM is an open source CFD program, a C++ object-oriented library that can perform in single-phase and multi-phase flows by using the Volume of Fluid (VOF) method. The continuity, momentum, and energy equations are solved in the compressibleInterFoam solver in OpenFOAM.

4.2.1 Mesh generation and mesh independence analysis

The mesh generation has done by using snappyHexMesh utility supplied by OpenFOAM. This snappyHexMesh tool generates 3D meshes that are in the Stereolithography (STL) or Wavefront Object (OBJ) format from triangular surface geometries (Greenshields, 2015).

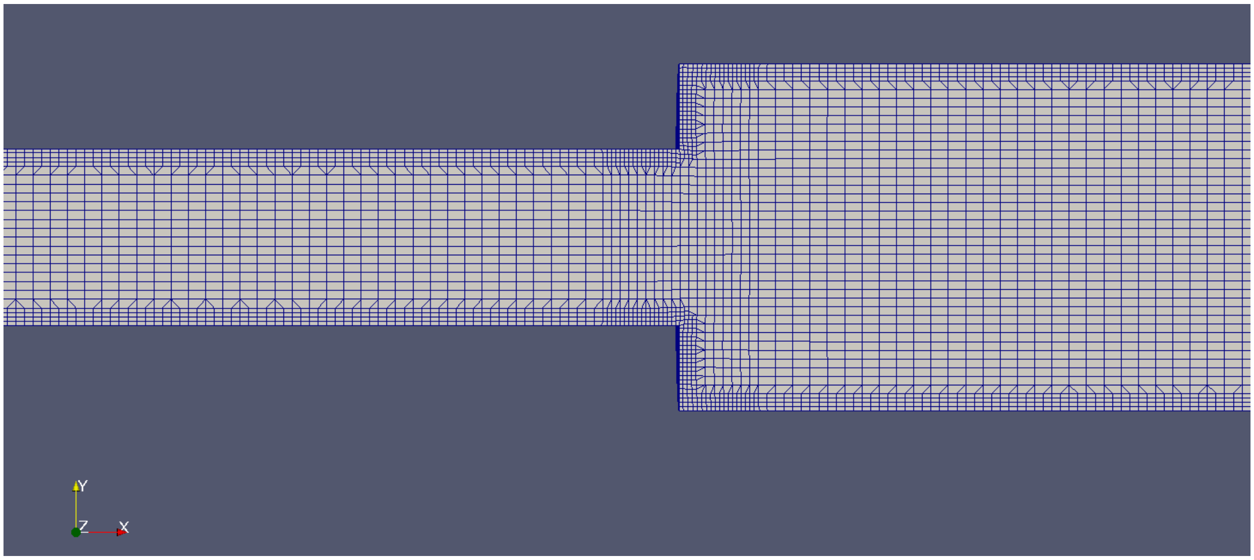

Figure 4. 11: The mesh appearance near the weir

Mesh independence analysis was done by using three mesh resolutions which have 0.2 million, 1.5 million, and 5.6 million cells in total. When the total cell number is 1.5 million cells and 5.6 million cells, the mesh converged to the experimental results as indicated in Figure 4.12. Therefore, in this study, intermediate mesh size was used in the numerical model.

In the second part of the CFD investigation, a geometry that was 10 times larger than the experimental apparatus was been created in the OpenFOAM. The goal of this work was to evaluate scale effects in the formation of entrapped air pockets. The geometry characteristics (i.e. cell count) was equivalent to the intermediate mesh size used in the comparisons presented in the results section.

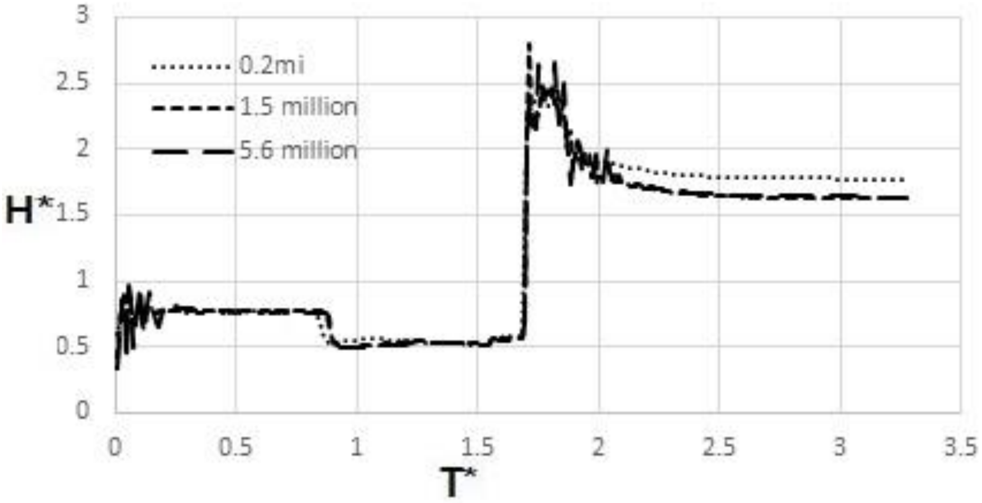

Figure 4. 12: Mesh independence analysis

4.2.2 Rigid-Column modeling

To obtain an independent comparison of the cavity celerity and the flow velocity upon the opening of the upstream valve, a lumped-inertia approach is proposed. By neglecting spatial variations of pressure gradient, a rigid column approach model can be developed, as shown in in Wylie and Streeter (1993). At the earlier stages of the experiment, when a cavity is propagating following the opening of the upstream air valve, the cavity motion can be expressed by $C_{air} = C_i\sqrt{gD}$, with C_i changing with the cavity thickness, and assuming a maximum value of 0.542 for a fully open pipe.(Vasconcelos and Wright 2008). When the upstream valve is opened, it is assumed that the water column between the reservoir and the leading edge of the air cavity will undergo an acceleration that can be described as:

$$\frac{dV}{dt} = \frac{g}{L_C}\left[Y_0 - Y_2 - \left(K + f\,\frac{L}{D}\right) * \left(\frac{Q^2}{2gA^2}\right)\right] \tag{4.1}$$

Where L_C is the length of the rigid-column, Y_0 is the water level at the upstream reservoir, Y_2 is the water level at the downstream end of the pipe when cavity advance through the pipe, K is the loss due to the entrance and the discharge which is 1 for the fully open case but assumed as 5 for the partially open cases, f is the friction loss, Q is the flow rate caused by the rigid-column assumed as 0 before opening upstream valve, A is the pipe area. Velocity results from this equation are then compared to correspondent velocity values yielded by the CFD model.

4.2.3 Threshold for air pocket entrapment

An expression was proposed by Li and McCorquodale (1999) to assess whether a rapid filling pipe condition that involve relative velocities between air and water phases could evolve into the development of shear flow instabilities and air pocket entrapment. In this study, instabilities would develop is an interfacial Froude-like variable that depend on the relative free surface flow velocity V_{FS} and the air velocity V_a would exceed a critical value F_c that depends on the depth of the water in the free surface flow H_{water}, the density ρ of water and air phases, and the surface water wave length λ:

$$F_I = \frac{V_a + V_{FS}}{\sqrt{gH_{water}}} \geq F_c \tag{4.2}$$

$$F_c = K_f \sqrt{\frac{\lambda}{2\pi H_{water}}} * \sqrt{\left(1 - \frac{\rho_{air}}{\rho_{water}}\right) * \left(\frac{\rho_{water}}{\rho_{air}} \tanh\left(\frac{2\pi H_{air}}{\lambda}\right) + \tanh\left(\frac{2\pi H_{water}}{\lambda}\right)\right)} \tag{4.3}$$

Where F_I is the interfacial Froude number; F_c is the critical Froude number; V_a is the air velocity which is equal to the pressurization bore velocity; V_{FS} is the free surface velocity; H_{water} is hydraulic depth of water=A_{water}/T_{fs}; A_{water} is the cross sectional area of the water flow; T_{fs} is the free surface width; H_{air} is the hydraulic depth of air = $(A_{pipe} - A_{water})/T_{fs}$; K_f is the Froude number correction factor, defined as:

$$K_f = K_T \left[1 - \frac{0.4\, H_b/H_w}{1 + \frac{1\delta B}{2\delta y}\frac{0.4 H_b}{B}}\right] \tag{4.4}$$

Where B is the top width, y flow depth, $\frac{\delta B}{\delta y}$ is the rate of change of B and H_b is the wave height.

Two Critical Froude number was calculated: $\mathrm{Fc_{high}}$ and $\mathrm{Fc_{low}}$. λ is the wave length that can vary from 20mm (for capillary waves) to several time Yu which is the effect of the pipe length that is incorporated in a modified wave length.

$$Y_u = Y_1 + 5 * 10^{-6} * L * F_i \tag{4.5}$$

According to this criterion, when F_I has a value higher than F_c, air pocket formation may occur. Figure 4.12 illustrates the calculated values of $\mathrm{F_C}$ and $\mathrm{F_I}$ for two of the conditions tested in the experiments: 27-mm weir opening, and either 0.914-m pressure in the upstream reservoir or 0.305-m pressure in the upstream reservoir for varying water depths at the flow region behind the air cavity.

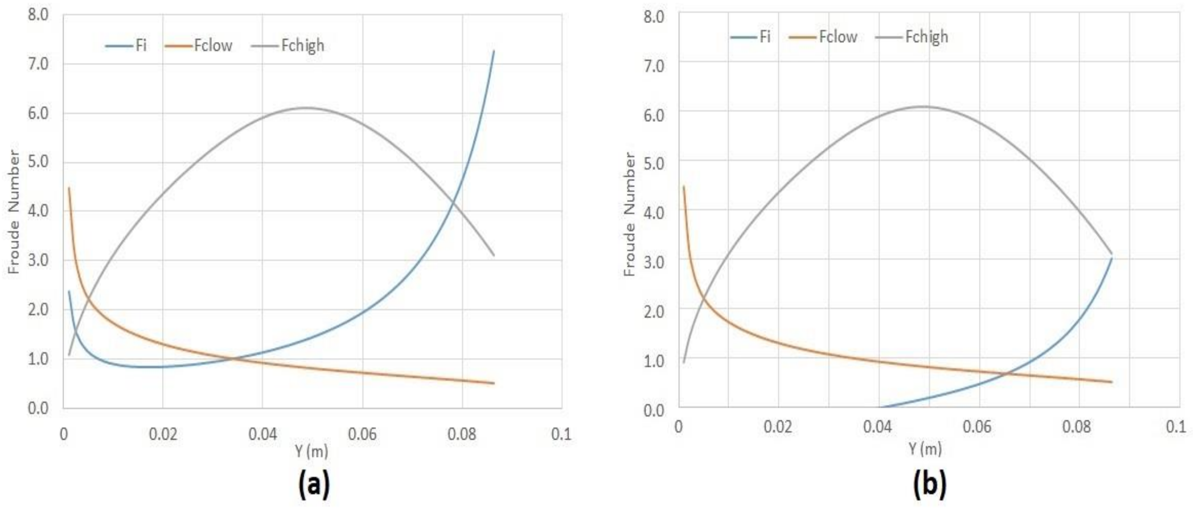

Figure 4. 13: The results of threshold for (a) an air-pocket entrapment case: 27mm opening under 0.914-m pressure (b) no air-pocket entrapment case: 27mm under 0.305-m pressure

Kordyban (1990) developed a comparable expression for the air-water instabilities to develop (Equation 4.5):

$$\rho_G U_G^2 \geq g(\rho_L - \rho_G) h_G \tag{4.6}$$

Where ρ_G is the gas density, ρ_L is the density of the liquid, $h_G$is the height of the gas, and U_G is the velocity of the gas. However, this relationship overpredicts the critical gas velocity by a factor of two. Therefore, the criteria below was used to determine the possibility of air pocket entrapment.

$$U_G - U_L \geq \frac{1}{2}\sqrt{\frac{(\rho_L - \rho_G) g h_G}{\rho_G}} \tag{4.7}$$

Chapter 5

Results and Discussion

5.1 Experimental Results

In the experimental study, air entrapment was investigated in 12 cases with the various downstream height of the weir and with three peaks of pressure head at the upstream reservoir. In some cases air entrapment was observed as result of an SFI process as the upstream valve was opened and rapidly pushed air over the water phase. However, in some other cases, the water inflow developed into a pipe-filling bore that pushed air all the way toward the downstream end of the apparatus, but no pocket entrapment was observed. The outcomes (Bore or PE – pocket entrapment) for each one of the 12 cases are shown in Table 5.1, and these are compared to the CFD predictions and Li and McCorquodale (LM) expression. Additionally, bore velocities, which were observed to increase with the upstream reservoir pressure, are presented in Table 5.2.

Table 5. 1: Observed & CFD & Li and McCorquodale outcomes of the rapid filling of the conduit.

	Discharge opening at downstream end				
Upstream reservoir pressure head (m)	Results for:	Full	38 mm	27 mm	20 mm
0.305	LM	Bore	Bore	Bore	PE
	CFD	Bore	Bore	Bore	PE
	EXP	Bore	Bore	Bore	PE
0.610	LM	Bore	PE	PE	PE
	CFD	Bore	PE	PE	PE
	EXP	Bore	Bore	Bore	PE
0.914	LM	Bore	PE	PE	PE
	CFD	Bore	PE	PE	PE
	EXP	Bore	Bore	PE	PE

Table 5. 2: Observed and predicted pipe-filling bore celerity (m/s) upon opening of upstream valve

	Observed and simulated bore velocities (m/s) upon opening of upstream valve				
Upstream reservoir pressure head (m)	Results for:	Full	38 mm	27 mm	20 mm
0.305	CFD	1.6	3.2	3.64	NA
	EXP	1.9±0.1	2.5±0.1	3.4±0.2	NA
0.610	CFD	2.6	NA	NA	NA
	EXP	2.3±0.1	3.5±0.2	4.2±0.3	NA
0.914	CFD	3.2	NA	NA	NA
	EXP	2.4±0.1	4.8±0.2	NA	NA

Figure 5.1 presents the bore motion though the latest pipe is shown for fully open pipe under 0.915-m upstream reservoir pressure head. In this condition, there is no pocket entrapment observed in both experiment and CFD simulation.

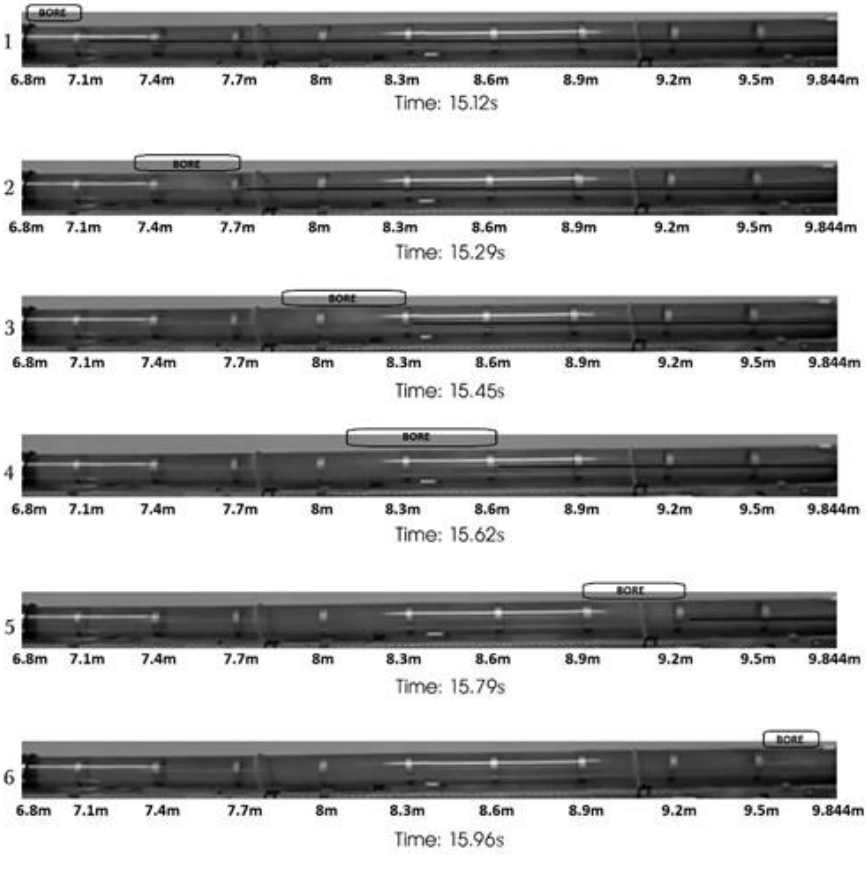

Figure 5. 1: Tracking bore in experimental observation after opening upstream valve under 0.914 m pressure fully-open case.

Figure 5.2 illustrates the pocket formation in the experiment for the condition with 27 mm opening and 0.914-m pressure head. In this condition, both experiment and CFD simulation agreed with pocket formation. The first pocket formation was observed at about 50% of the pipe, and the tail end of the pocket is shown in Figure 5.3. One can see that the increase at the air pressure at the location of first pocket forms pushes the air interface downward, decreasing the water depth.

As indicated in Li and McCorquodale (1999), the SFI mechanism may lead to a sequence of air pocket entrapment. There are three pockets formed in the experiment that shown in Figure 5.2. After some time, it was observed that the first pocket's leading edge and second pocket's tail, and second pocket's leading edge and third pocket's tail came together, and they created a long-thin one pocket that stayed in the pipe. This process of air pocket merging was observed in the CFD simulation results, as shown in Figure 5.4. More details on the CFD modeling results are presented in the subsequent section.

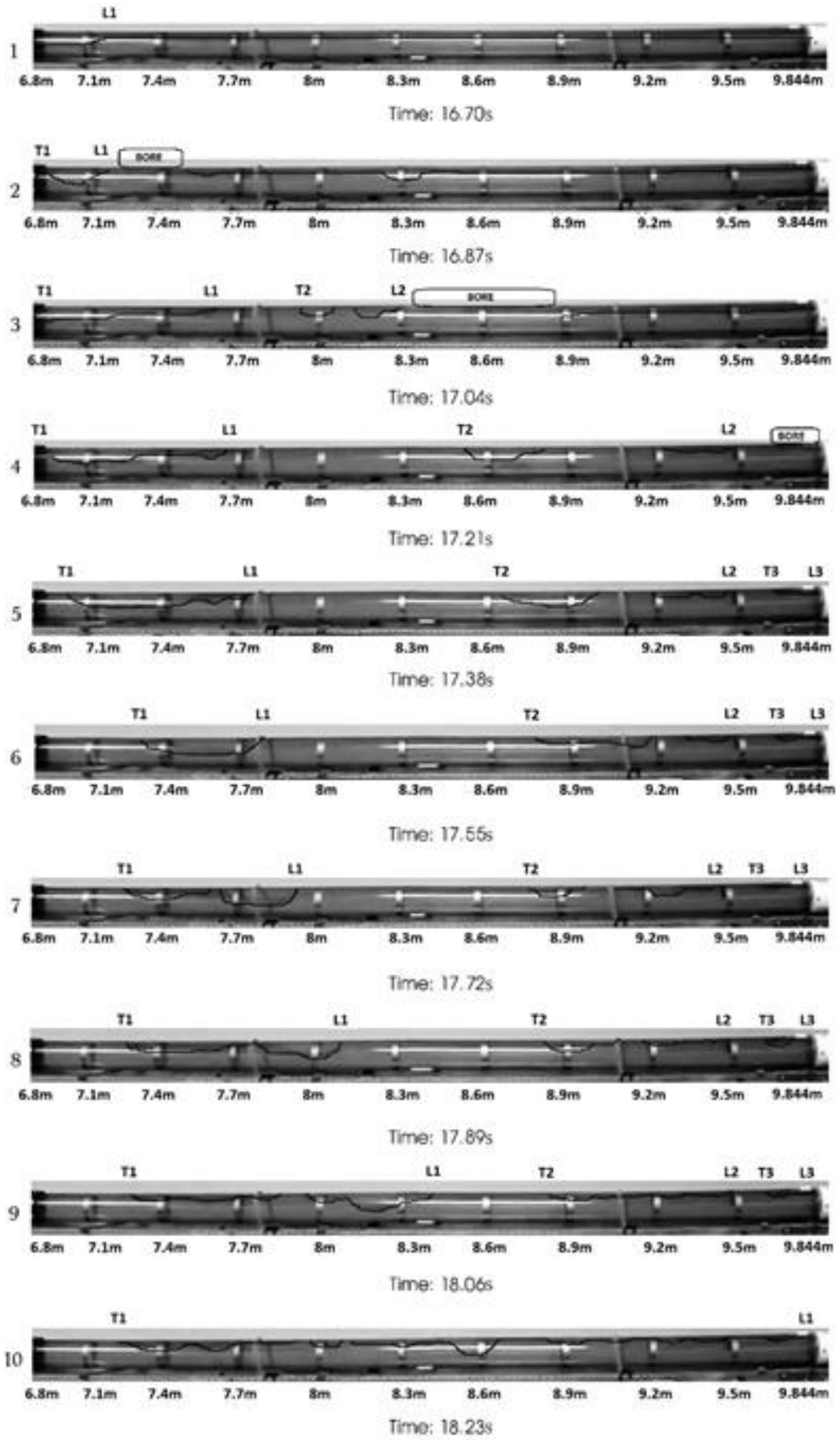

Figure 5. 2: Pocket formation at the latest pipe for 27mm opening under 0.914-m pressure head

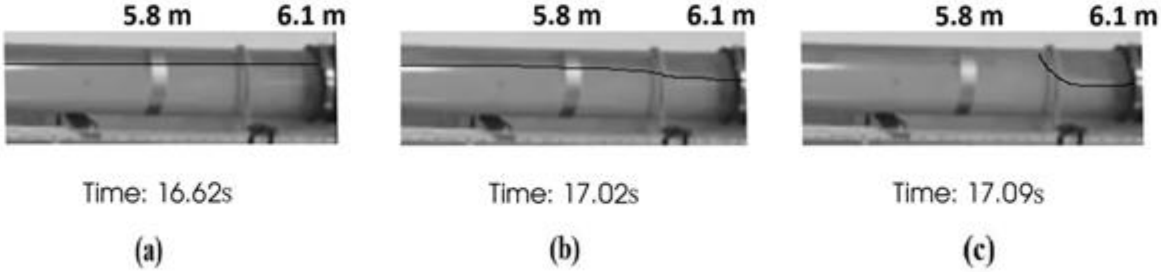

Figure 5. 3: The water level change at the location of first pocket forms for 27mm opening under 0.914-m pressure head

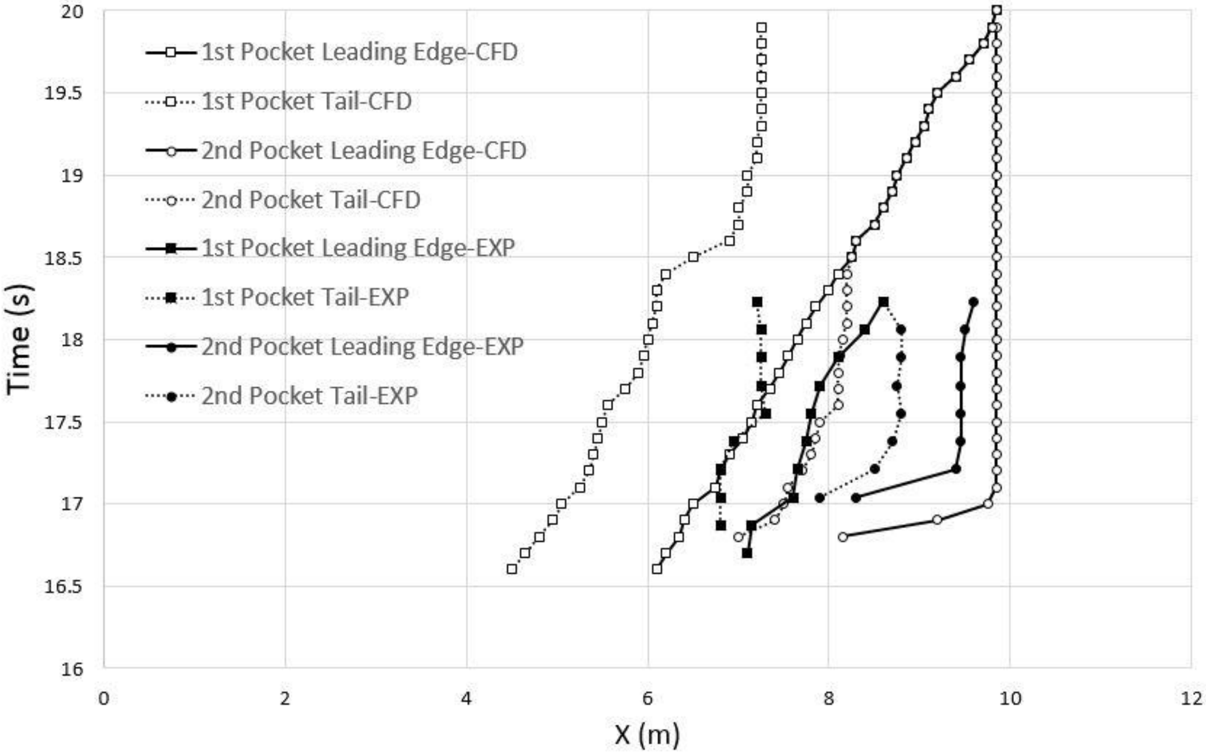

Figure 5. 4: Pocket formation comparison for CFD and Experimental Results for 27mm opening under 0.914-m pressure head case

5.2 CFD Modeling Results

Velocity, pressure, temperature, and air-water distribution results were obtained with the CFD model, and these results can be retrieved using tools such as Parafoam and scripts that allow for the calculation of results such as the maximum volume of entrapped air pocket. Figure 5.5 shows the thickness and the shape of the leading edge of the cavity at the location of the air cavity after 5 seconds of the opening downstream end valve. It is measured concerning the upstream valve. Not surprisingly, the celerity of the cavity decreases with a decrease in the cavity thickness. Cavity thickness at this location is presented in Table 3 and it was based on CFD results. Theoretical celerity calculated based on this cavity thickness is based on the Figure 2.3 results

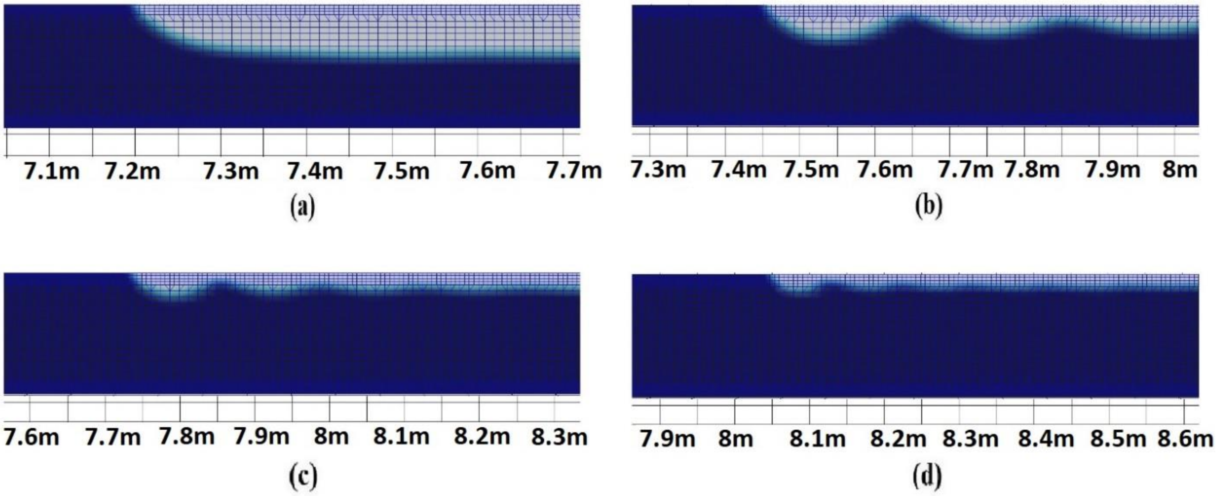

Figure 5. 5: Comparative advance of cavity at 5 sec. Pipe openings are: (a) full opening: at 7.25 m from upstream valve; (b) 38 mm opening: at 7.5m from upstream valve; (c) 27mm opening: at 7.8m from upstream valve); (d) 20mm opening: at 8.1m from upstream valve.

.Table 5. 3:Air-cavity characteristics

Opening	Thickness of Air (m)	Theoretical cavity Celerity (m/s)	Average CFD cavity celerity (m/s)	Cavity Volume (L)	Normalized Cavity Volume
Full	0.048	0.50	0.51	26.12	1.033
38 mm	0.019	0.47	0.48	8.09	0.270
27 mm	0.014	0.44	0.4	4.39	0.129
20 mm	0.011	0.39	0.31	2.44	0.0657

As is shown in Table 5.3, air cavity celerity based on the expressions presented in the literature review were in general close to corresponding results obtained with the CFD tool. As explained earlier, once the upstream valve was opened a sudden increase in the velocity and the pressure in the pipe was recorded. These changes in flow conditions were also detected in the CFD simulation results, as is shown in Figures 5.6, 5.7, and 5.8. Following the complete filling of the pipe the flow velocity drops because all the pipe surface is in contact with the moving flow and creates friction losses. As means of comparison, CFD results are plotted alongside the simulated results using the rigid-column model in Figures 5.6 and 5.7. For the partially-open cases the rigid column velocity exceeds the CFD results slightly, while worst predictions are noiced for the smallest weir (20mm opening cases). The reasons for this discrepancy are unknown at this point.

Pressure results are presented in Figure 5.8, where CFD results are compared with experimental measurements. It was noticed in the CFD results that when pockets were formed there was significant pressure oscillations in the results associated with the pocket release at the downstream end of the apparatus.

Unfortunately, due to the calibration and installation issues with the MicroADV flow velocity meter, it was not possible to obtain accurate experimental velocity results from the experiment. Instead of experimental results, we have used Rigid-Column method to check velocity results. However, comparison of experimental and CFD velocity results is also shown in Figure 5.9 and 5.10.

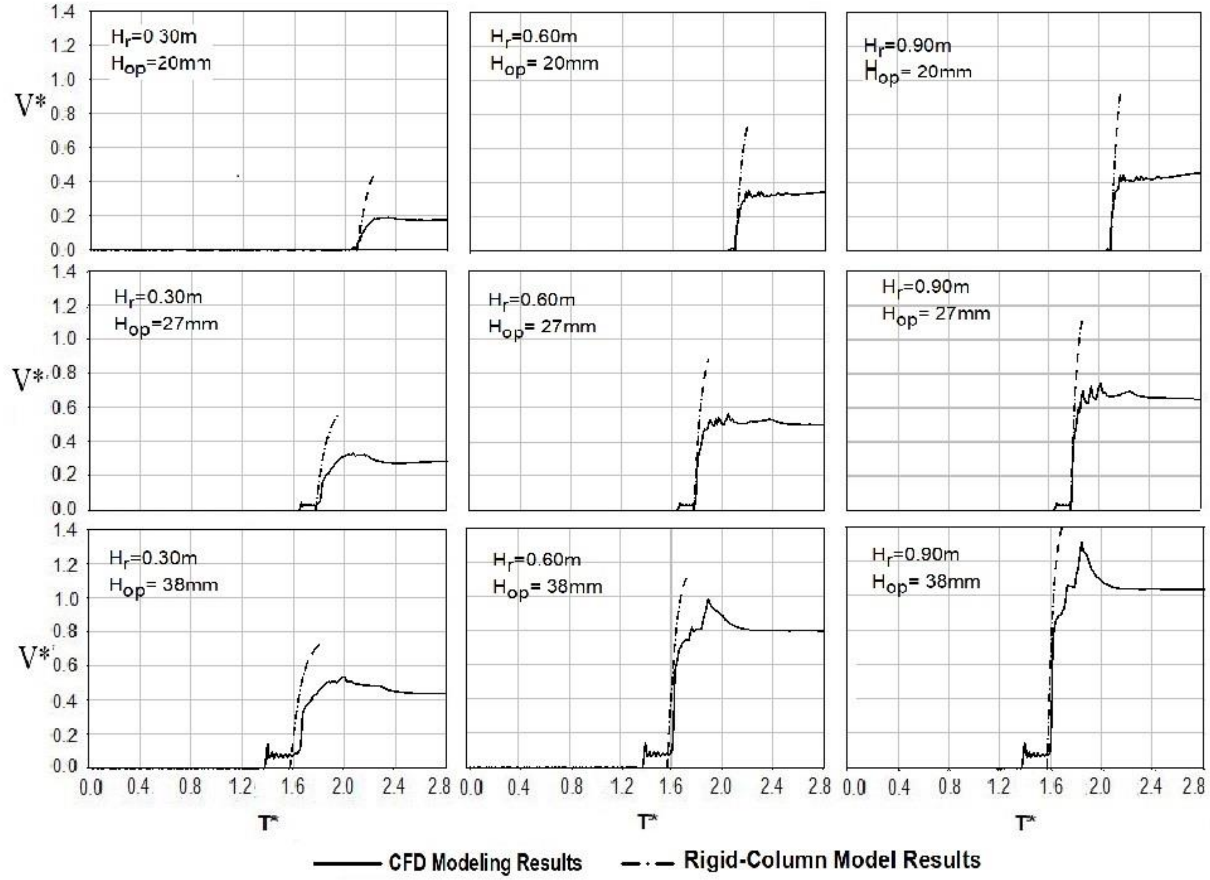

Figure 5. 6: Normalized velocity(V*) for partially open cases

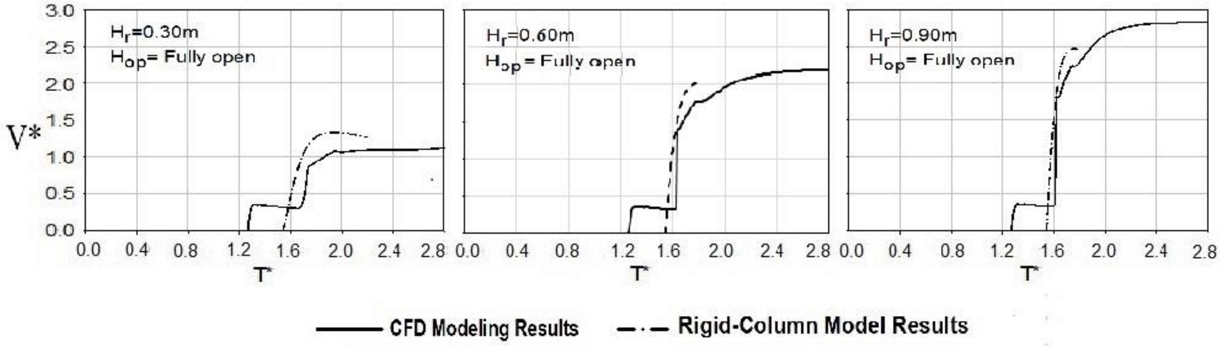

Figure 5. 7: Normalized velocity(V*) for fully open case

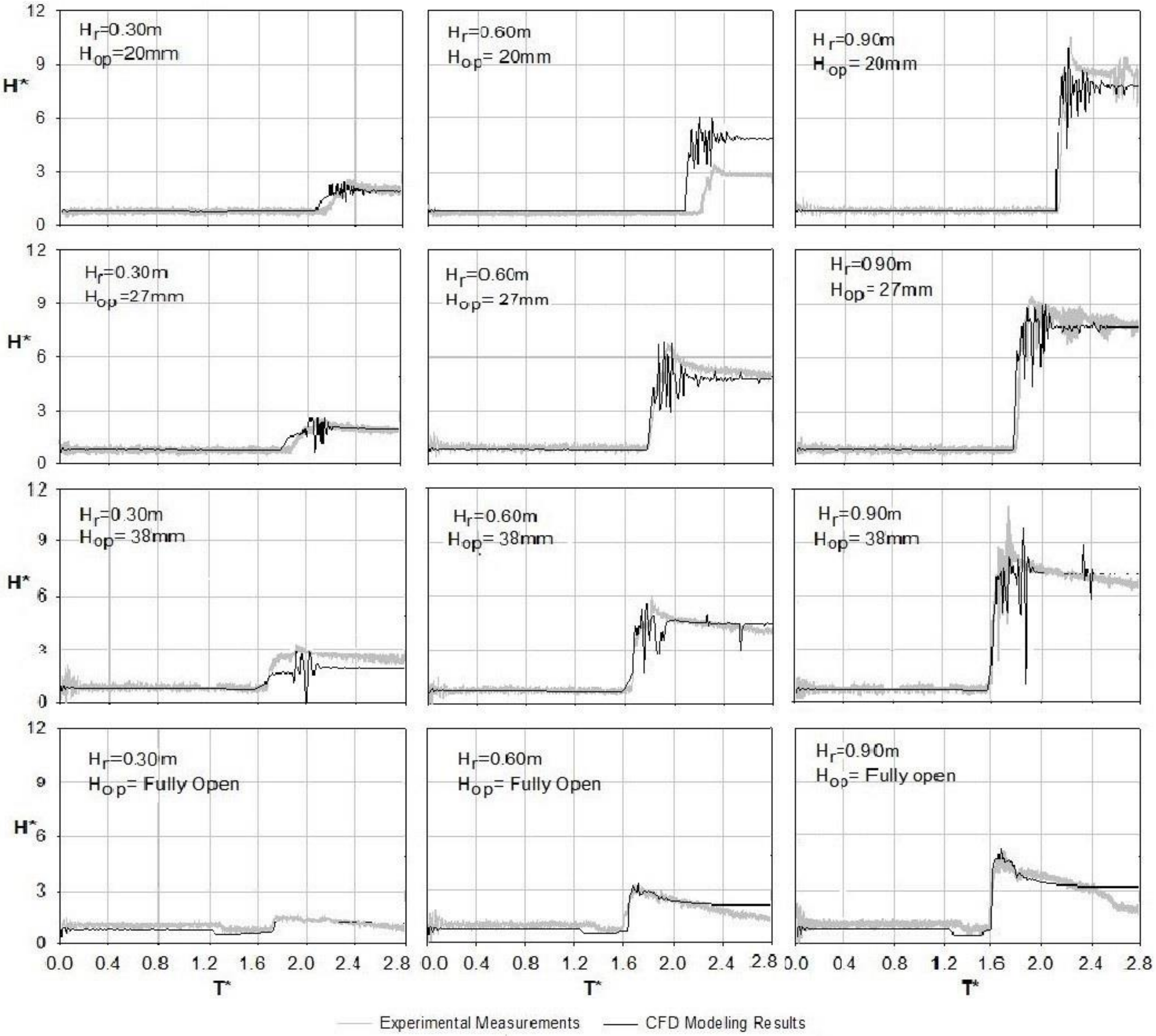

Figure 5. 8: Normalized pressure head (H*) for all tested conditions

One objective way to compare the accuracy between numerical modeling prediction and experimental results, or between two different modeling approaches, is through the calculation of a L_1 norm:

$$L_1 = \sum \left| X_{model} - X_{exp} \right| \tag{5.1}$$

Where X_{model} and X_{exp} correspond to pressure or velocity results obtained with the model or measured in the experiments for the same time instant. When the comparison is between two numerical models, the L_1 norm can be calculated as:

$$L_1 = \sum \left| X_{model\ 1} - X_{model\ 2} \right| \tag{5.2}$$

The opening upstream valve, air pocket formation/bore motion and eventual air pocket release occurs at non-dimensional times $t^* = t/(\frac{\sqrt{gD}}{L})$ ranging from 1.5 and 2.5 for partially-open cases and 1 and 2 for fully-open cases. The calculation of L_1 was performed thus only in these time ranges, and results are shown in Table 5.4 for the comparison between the CFD and Rigid Column model for the velocity results following the upstream valve opening. Within a given degree of opening at the downstream end, the general tendency is that L1 decreases with higher reservoir upstream head. In absolute terms, L_1 decreased with the degree of opening at the downstream end.

Table 5. 4: L1 Norm comparison velocity of Rigid-Colum Model and CFD

	Discharge opening at downstream end				
Upstream reservoir pressure head (m)	Results compared	Full	38 mm	27 mm	20 mm
0.3048	RC-CFD	13.19	4.91	2.73	2.42
0.6096	RC-CFD	10.04	3.72	2.30	2.06
0.9144	RC-CFD	8.62	3.72	2.16	2.55

A calculation for the L_1 norm for pressure results that reflects the difference between CFD and experimental results are presented in Table 5.5. The norm values were minimum for full opening conditions and maximum for the smallest opening condition. There was no clear trend between L_1 values and upstream reservoir head.

Table 5. 5: L1 Norm comparison pressure of experimental results and CFD

	Discharge opening at downstream end				
Upstream reservoir pressure head (m)	Results compared	Full	38 mm	27 mm	20 mm
0.3048	EXP-CFD	8.95	54.66	33.13	16.93
0.6096	EXP-CFD	18.46	36.35	56.41	97.44
0.9144	EXP-CFD	21.67	52.64	64.84	64.54

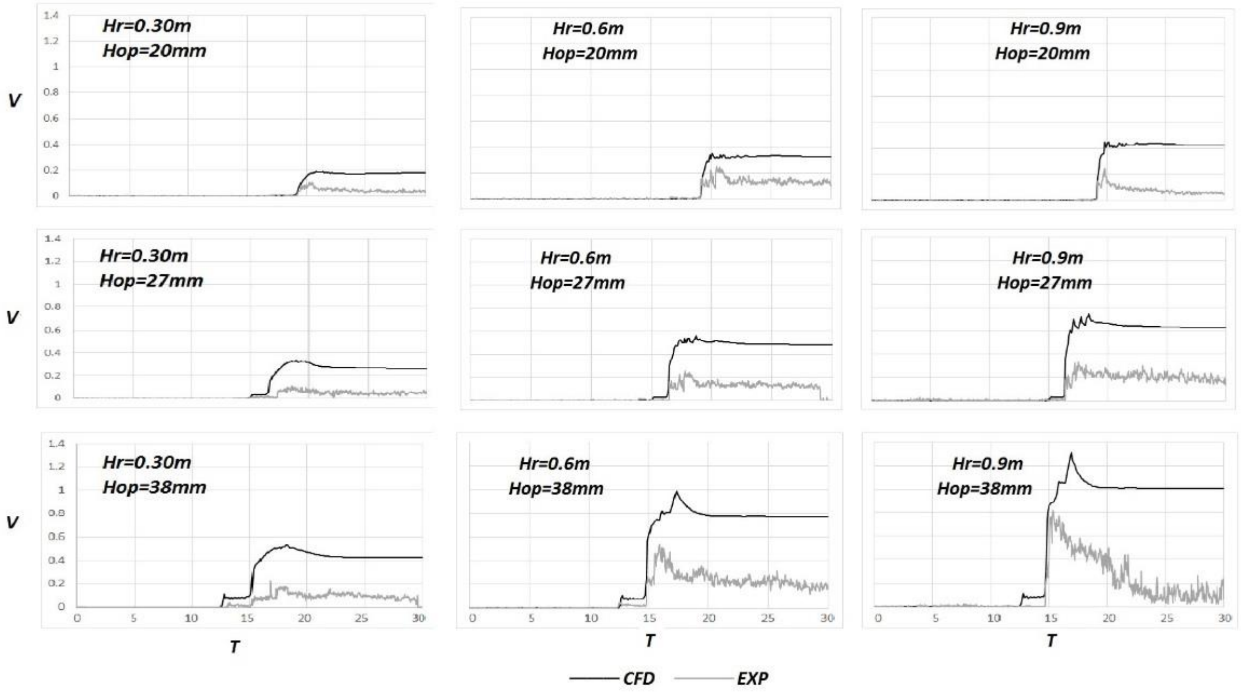

Figure 5. 9: Comparison of CFD and experimental velocity results for partially open cases.

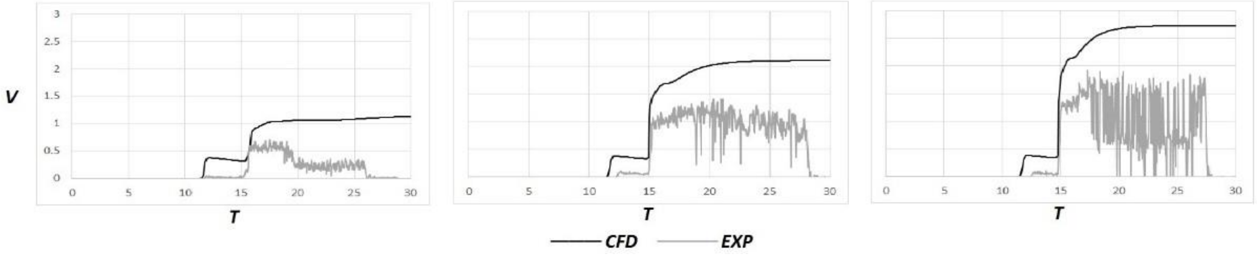

Figure 5. 10: Comparison of CFD and experimental velocity results for fully open cases.

Table 5.6 shows the maximum air cavity volume in the pipe; Table 5.7 illustrates the volume of entrapped air pockets and Table 5.8 presents the percentage of entrapped air captured from the maximum volume of air. As is seen from Table 5.8, when the cavity thickness decreases, and the pressure head increases, the percentage of the cavity that becomes entrapped as an air pocket increase, and indication of the faster propagation of the SFI over the pipe length.

Table 5. 6: Air Cavity Maximum Intrusion Volume (m3)

	Air Cavity Maximum Intrusion Volume (L)			
Upstream reservoir pressure head (m)	20 mm	27 mm	38 mm	Full
0.305	2.44	NA	NA	NA
0.610	2.44	4.39	8.09	NA
0.914	2.44	4.39	8.09	NA

Table 5. 7: Entrapped Air Pocket Volume (L)

	Entrapped Air Pocket Volume (L)			
Upstream reservoir pressure head (m)	20 mm	27 mm	38 mm	Full
0.305	1.88	NA	NA	NA
0.610	1.93	3.07	4.26	NA
0.914	2.05	3.50	5.07	NA

Table 5. 8: Percentage of Initial Cavity Volume Entrapped as an Air Pocket

	% of Initial Cavity Volume Entrapped as an Air Pocket			
Upstream reservoir pressure head (m)	20 mm	27 mm	38 mm	Full
0.305	77.01	NA	NA	NA
0.610	79.12	69.88	52.67	NA
0.914	84.09	79.80	62.74	NA

The percentage of maximum air intrusion and their discharges shown in Figure 5.11. In some cases, since the pressure is not enough to create a push to remove all air from the pipe, some air couldn’t be eliminated and stayed in the pipe.

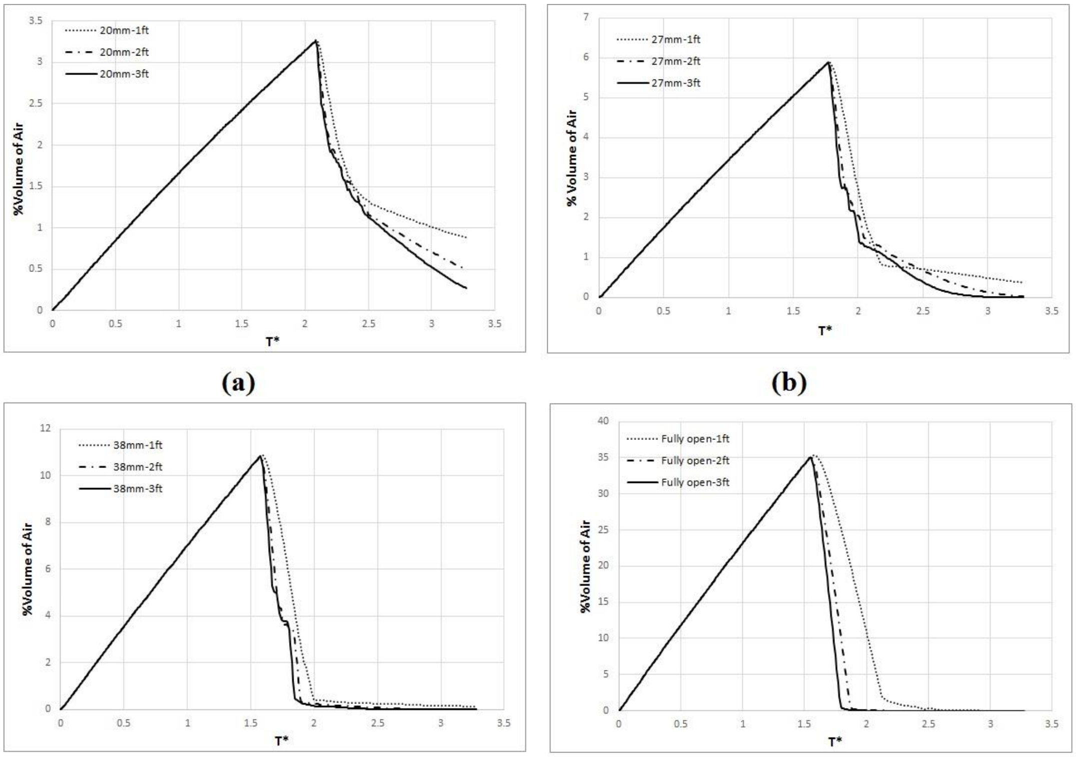

(a) **(b)**

(c) **(d)**

Figure 5. 11: Percentage of volume of Air during the process of cavity advance and subsequent air removal due to the opening of the upstream reservoir.

5.3 Results for Shear flow Instability Threshold

The instability threshold was created based on the criteria that proposed by Li and McCorquodale (1999). The threshold results were matched well with the CFD results. However, both CFD and McCorquodale determined pocket entrapment in some cases, when there is no pocket entrapment observation in the experiment. A comparison between different methods to assess the occurrence of SFI, including Kordyban (1990), is shown Table 5.9. It is noticed that Kordyban expression is the one that diverges most from the experimental observations, but in general CFD and Li and McCorquodale are in agreement. CFD tends to over predict air pocket entrapment, which in some sense is a conservative outcome that could be adequate in the context of tunnel filling analysis.

Table 5. 9: Air-pocket entrapment assessment

	Air Pocket Entrapment Assessment			
	Experimental	CFD	Kordyban	McCorquodale
20mm-0.305 m	Yes	Yes	No	Yes
20mm-0.610 m	Yes	Yes	Yes	Yes
20mm-0.914 m	Yes	Yes	Yes	Yes
27mm-0.305 m	No	No	No	No
27mm-0.610 m	No	Yes	Yes	Yes
27mm-0.914 m	Yes	Yes	Yes	Yes
38mm-0.305 m	No	No	Yes	No
38mm-0.610 m	No	Yes	Yes	Yes
38mm-0.914 m	No	Yes	Yes	Yes
Fully open-0.305 m	No	No	No	No
Fully open-0.610 m	No	No	No	No
Fully open-0.914 m	No	No	No	No

5.6 Pressurization Interface

It is possible to perform the tracking pressurization interface trajectory using the results of CFD simulations, and these trajectories are presented in Figures 5.12 to 5.23. Snapshots of the flow profiles are also presented, in some cases indicating the appearance of air pockets in the filling process. These air pockets also create a sudden “jump” in the pressurization interface trajectory, marking the formation of the air pocket and the migration of the pressurization interface further ahead. The trajectories for the CFD modeling conditions that did not resulted in pocket formation are presented in Figures 5.19 to 5.23. There is no break in the trajectory, and the advance simply reflects the motion of a pipe-filling bore.

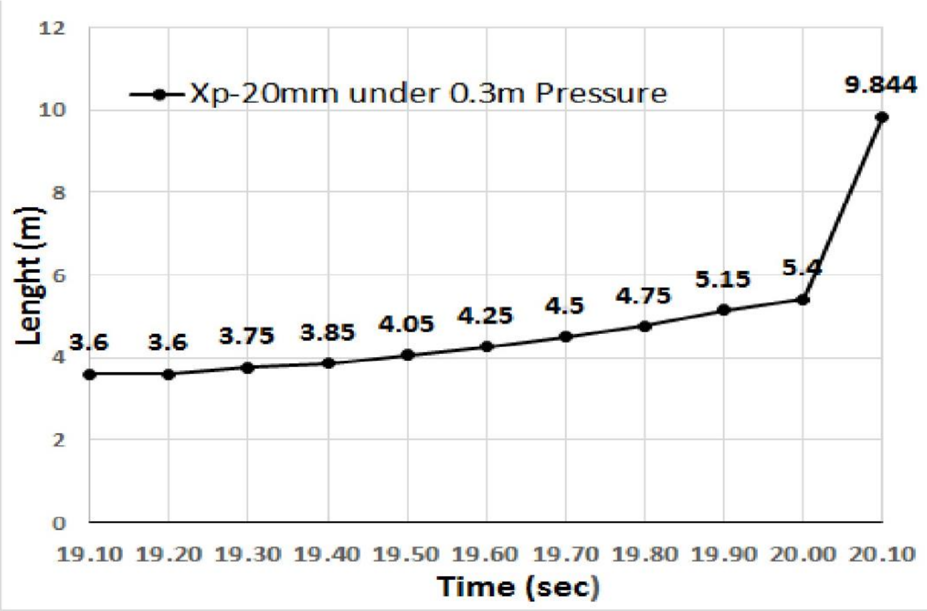

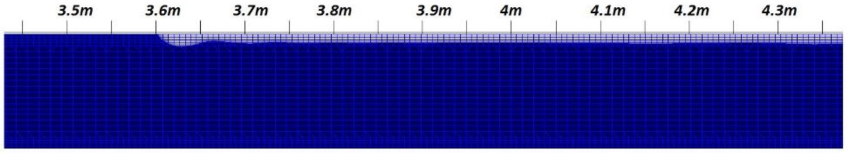

Time: 19.10s

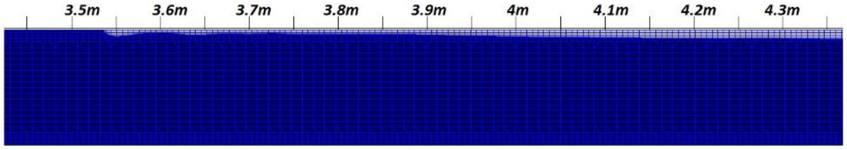

Time: 19.40s

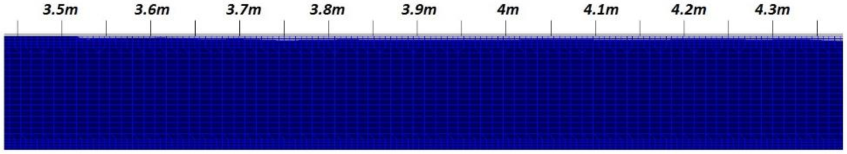

Time: 19.70s

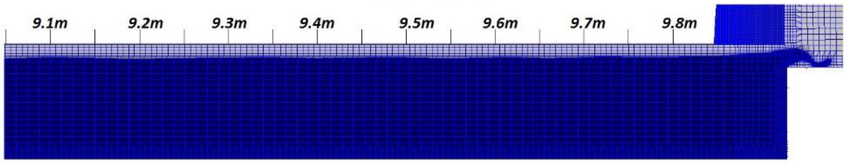

Time: 20.10s

Figure 5. 12: Pressurization interface coordinate (Xp) for 20mm opening under 0.305-m pressure head

Figure 5. 13:Pressurization interface coordinate (Xp) for 20mm opening under 0.610-m pressure head

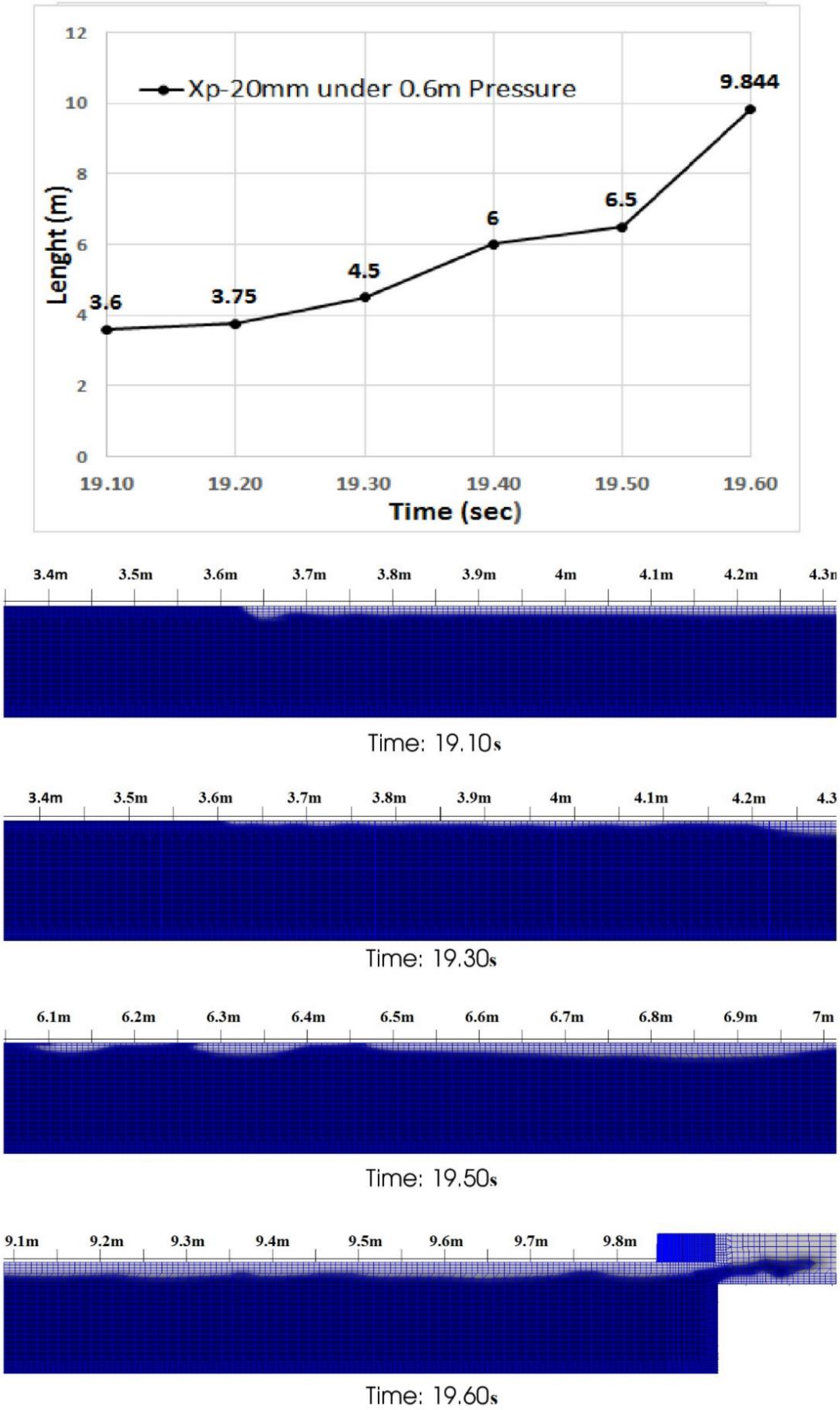

Figure 5. 13:Pressurization interface coordinate (Xp) for 20mm opening under 0.610-m pressure head

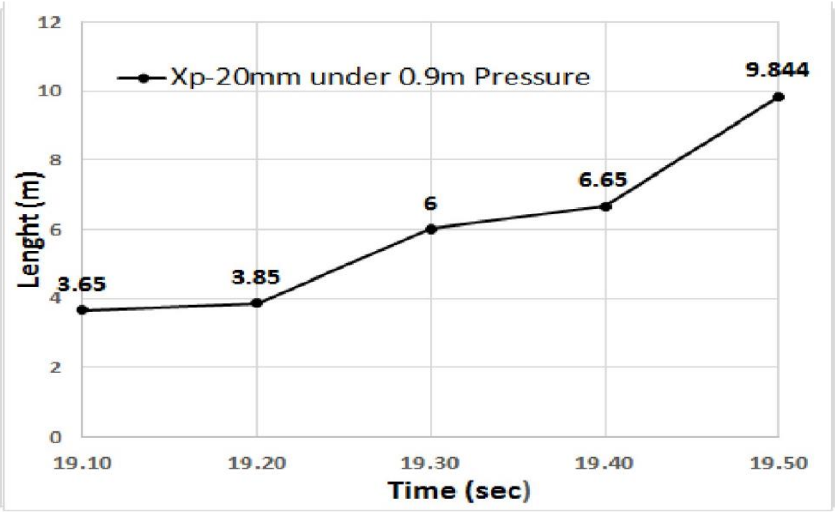

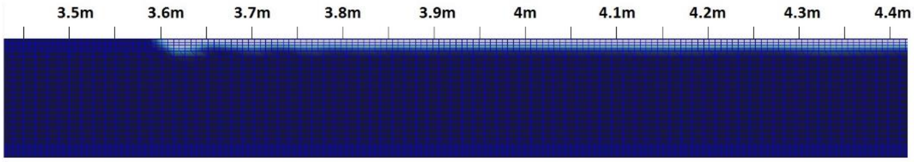

Time=19.1s

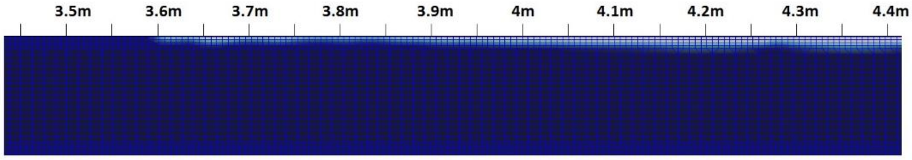

Time=19.2 s

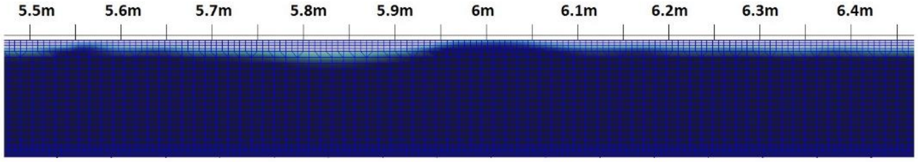

Time=19.3s

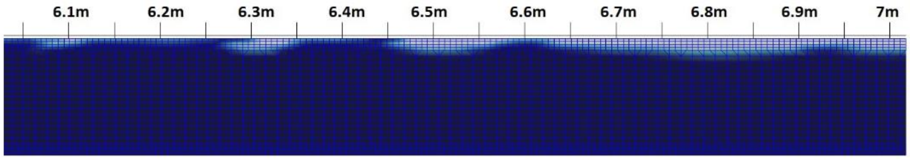

Time = 19.4s

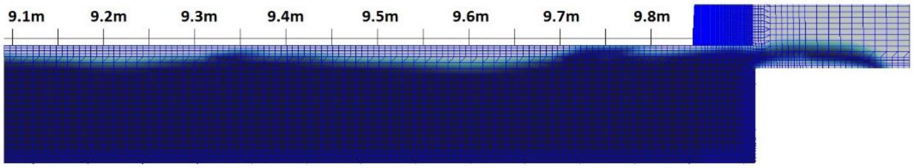

Time =19.5s

Figure 5. 14:Pressurization interface coordinate (Xp) for 20mm opening under 0.914-m pressure head

Figure 5. 15:Pressurization interface coordinate (Xp) for 27mm opening under 0.610-m pressure head

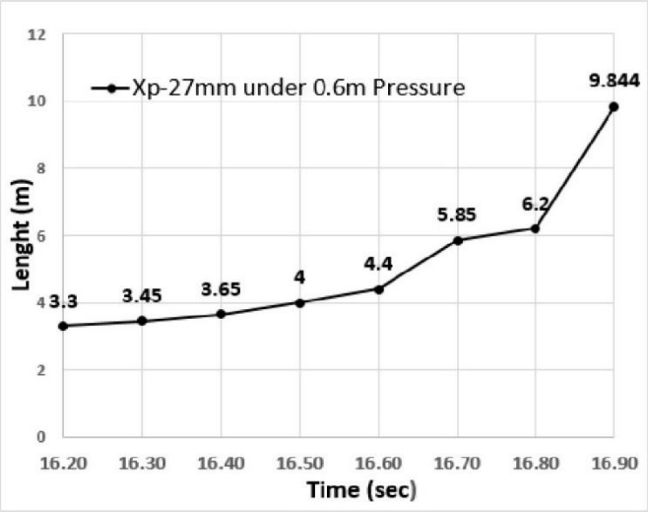

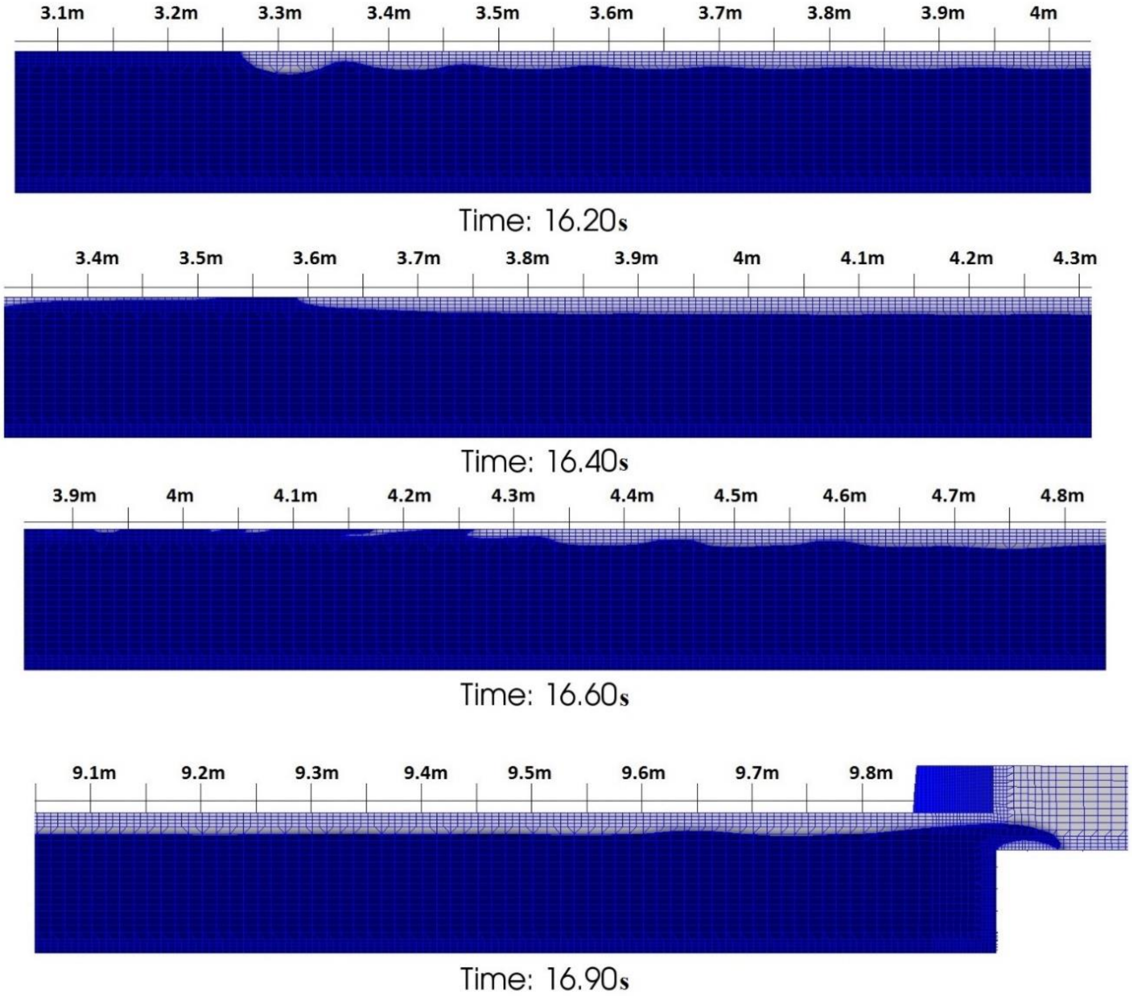

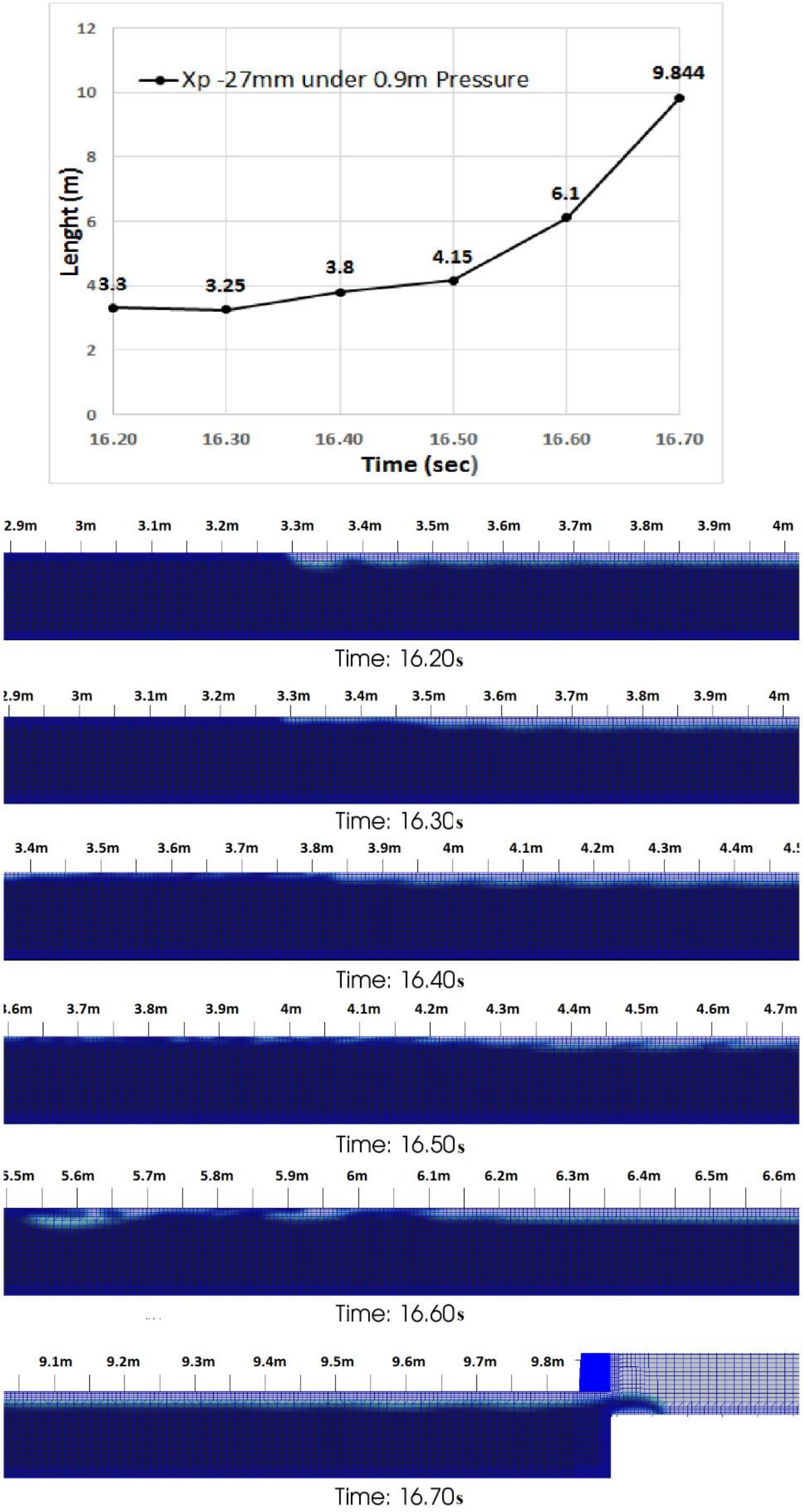

Figure 5. 16:Pressurization interface coordinate (Xp) for 27mm opening under 0.914-m pressure head

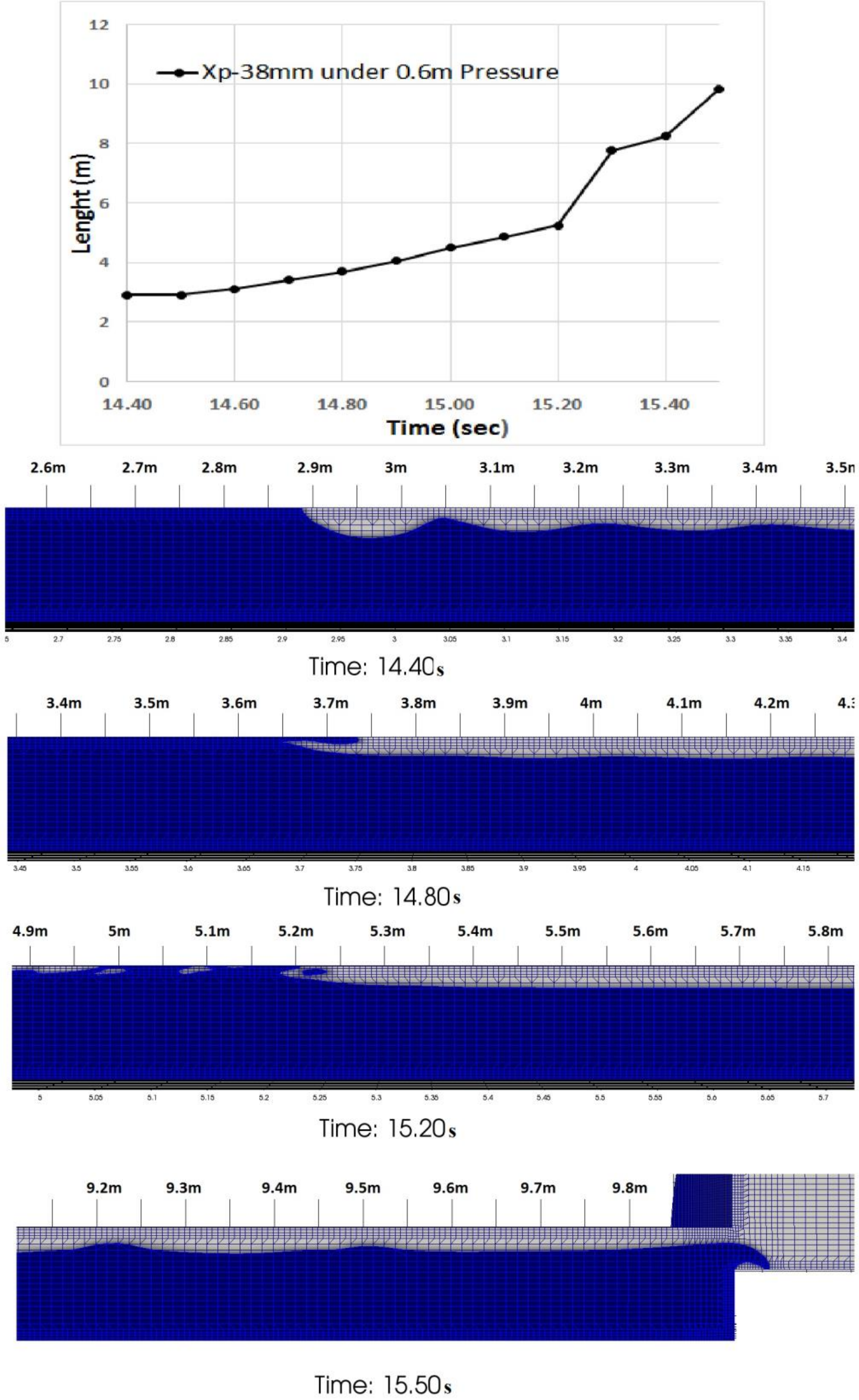

Figure 5. 17:Pressurization interface coordinate (Xp) for 38mm opening under 0.610-m pressure head

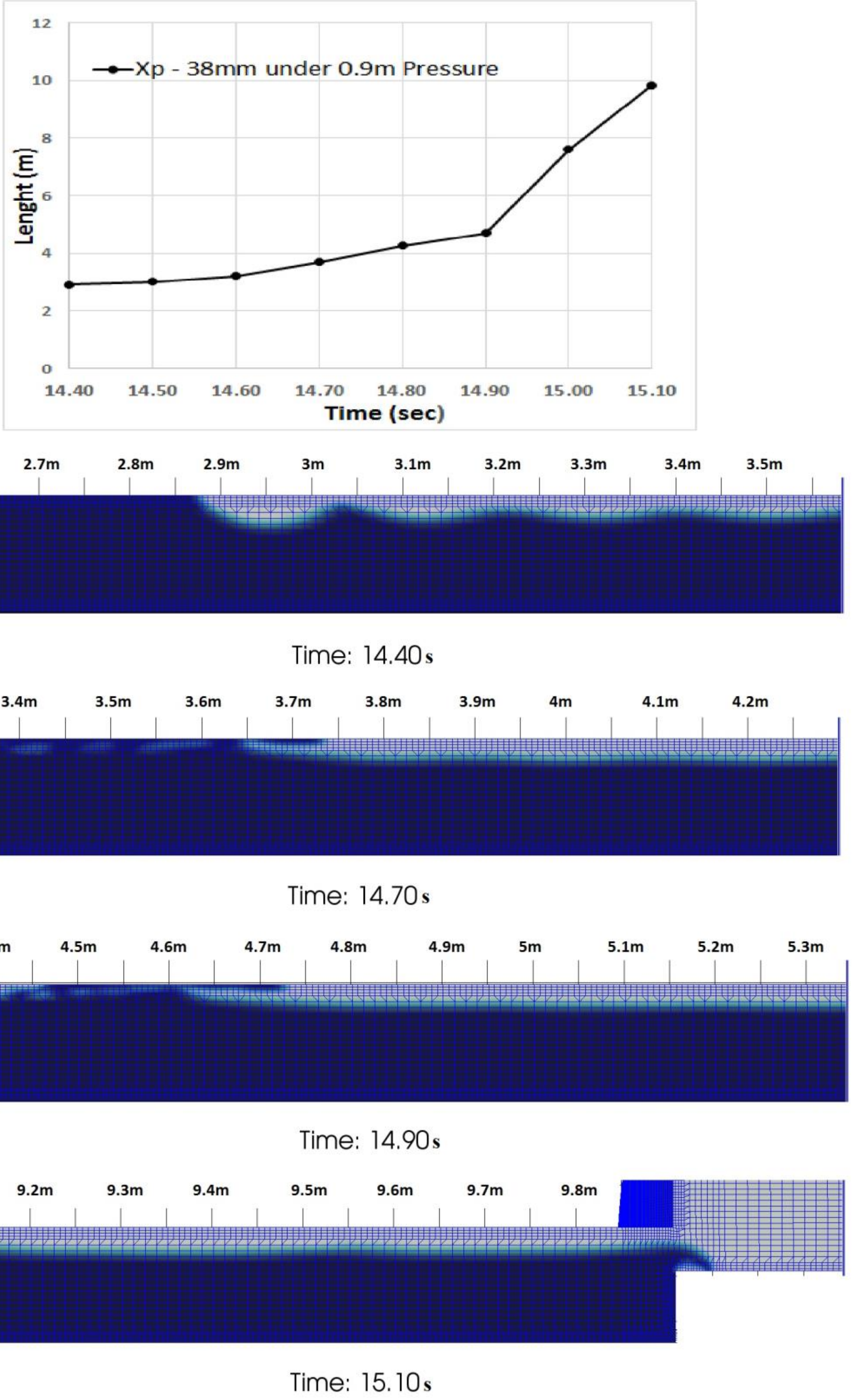

Figure 5. 18:Pressurization interface coordinate (Xp) for 38mm opening under 0.914-m pressure head

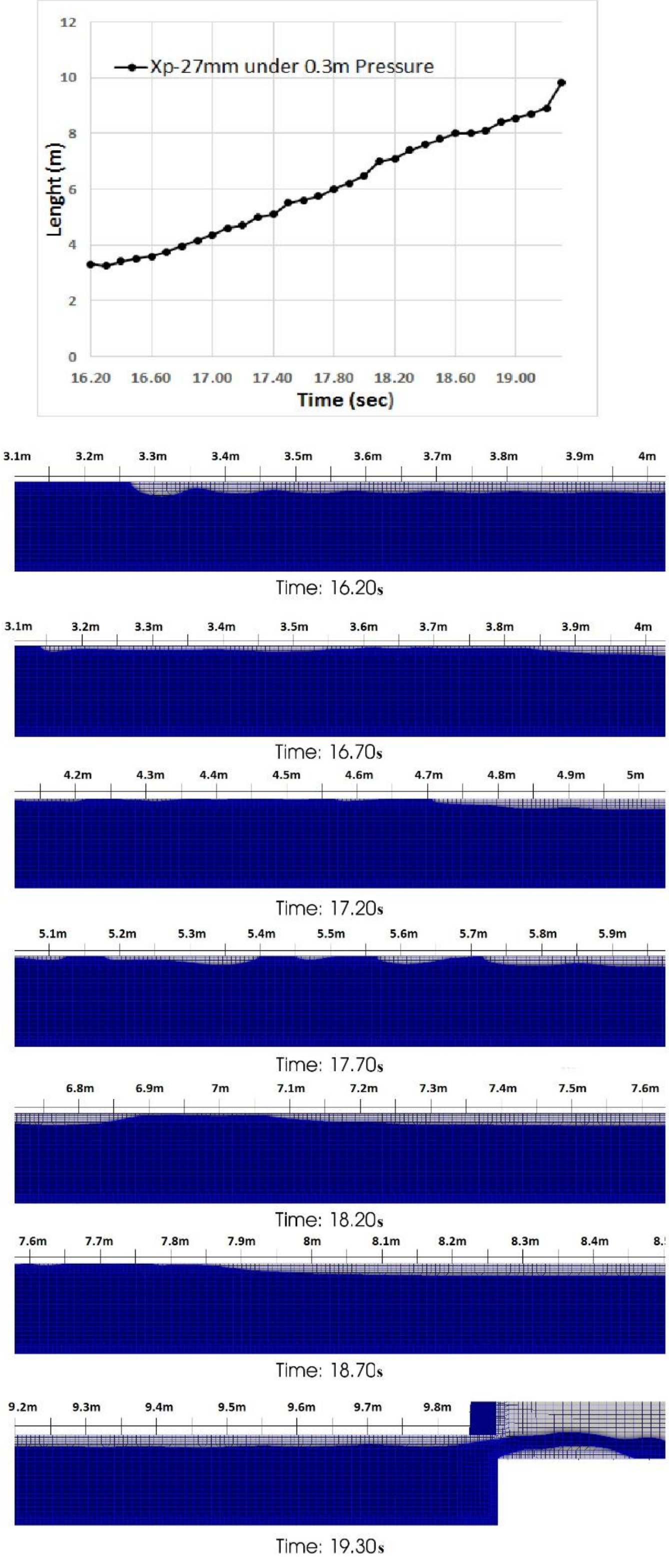

Figure 5. 19:The bore tracking for 27mm opening under 0.305-m pressure head

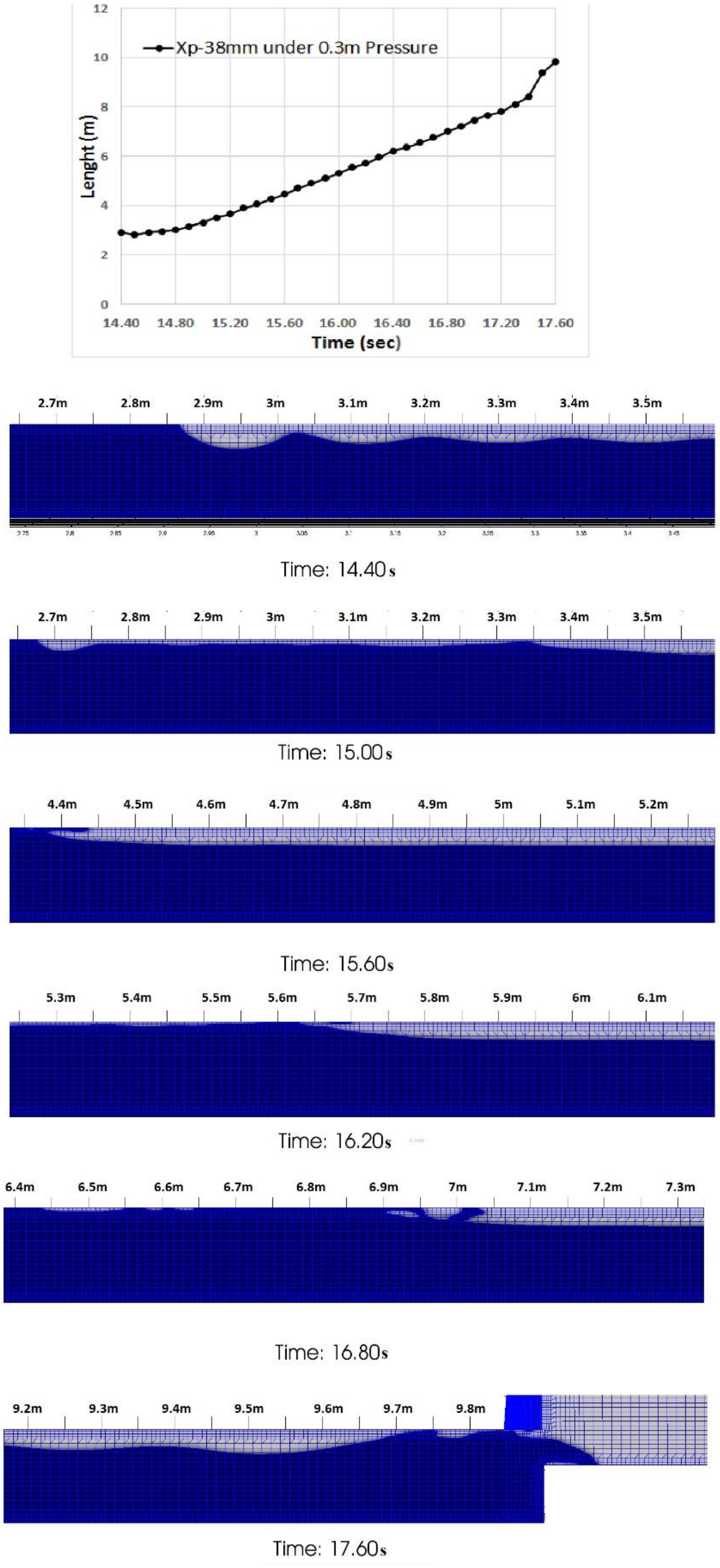

Figure 5. 20:: The bore tracking for 38mm opening under 0.305-m pressure head

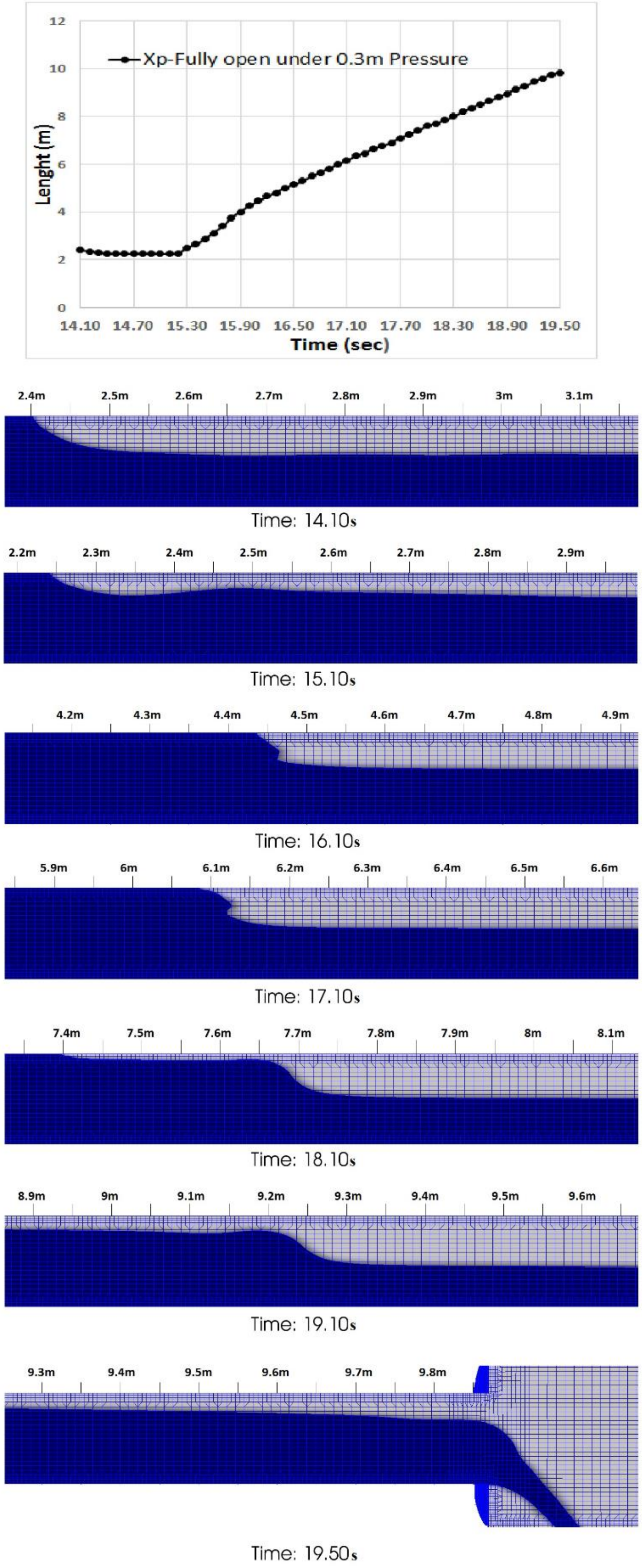

Figure 5. 21:The bore tracking for Fully open case under 0.305-m pressure head

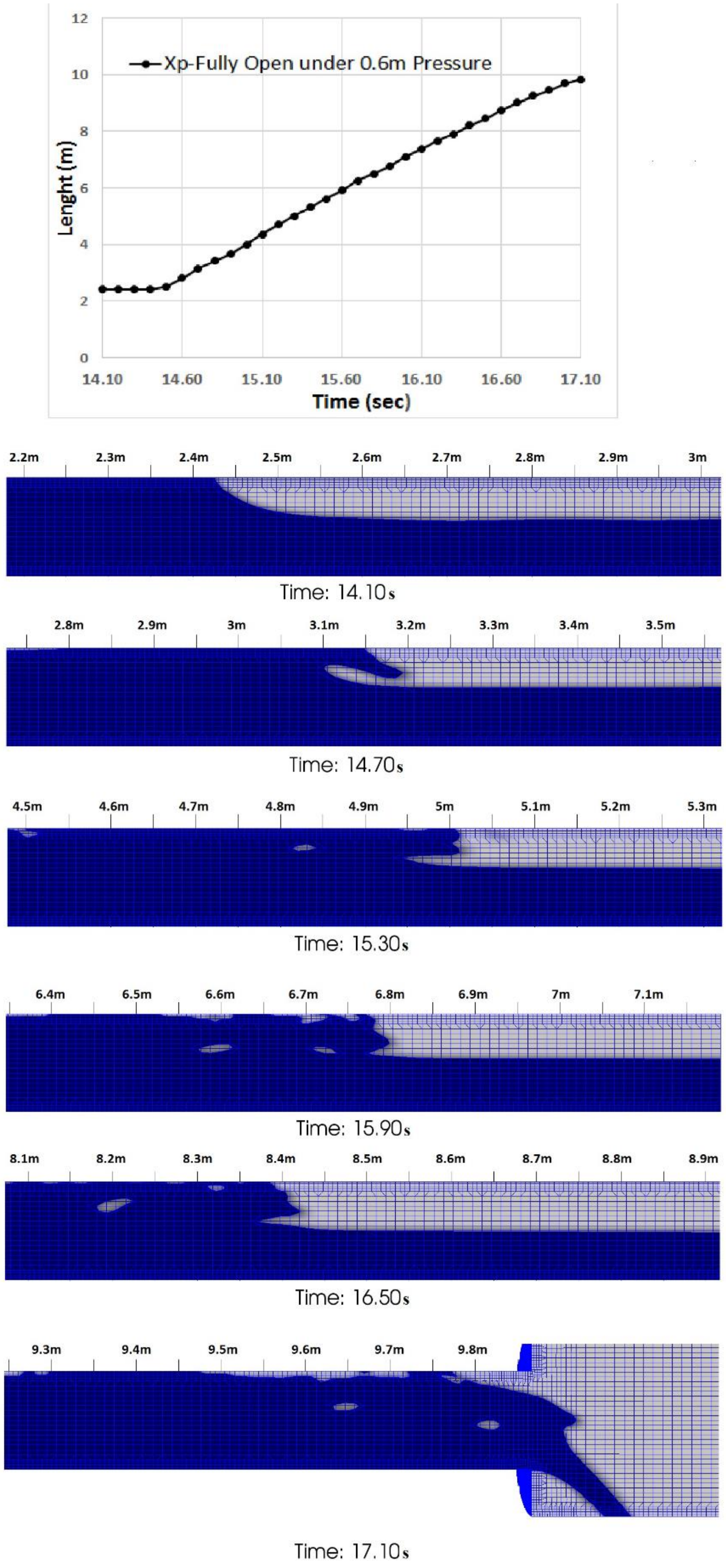

Figure 5. 22:The bore tracking for Fully open case under 0.610-m pressure head

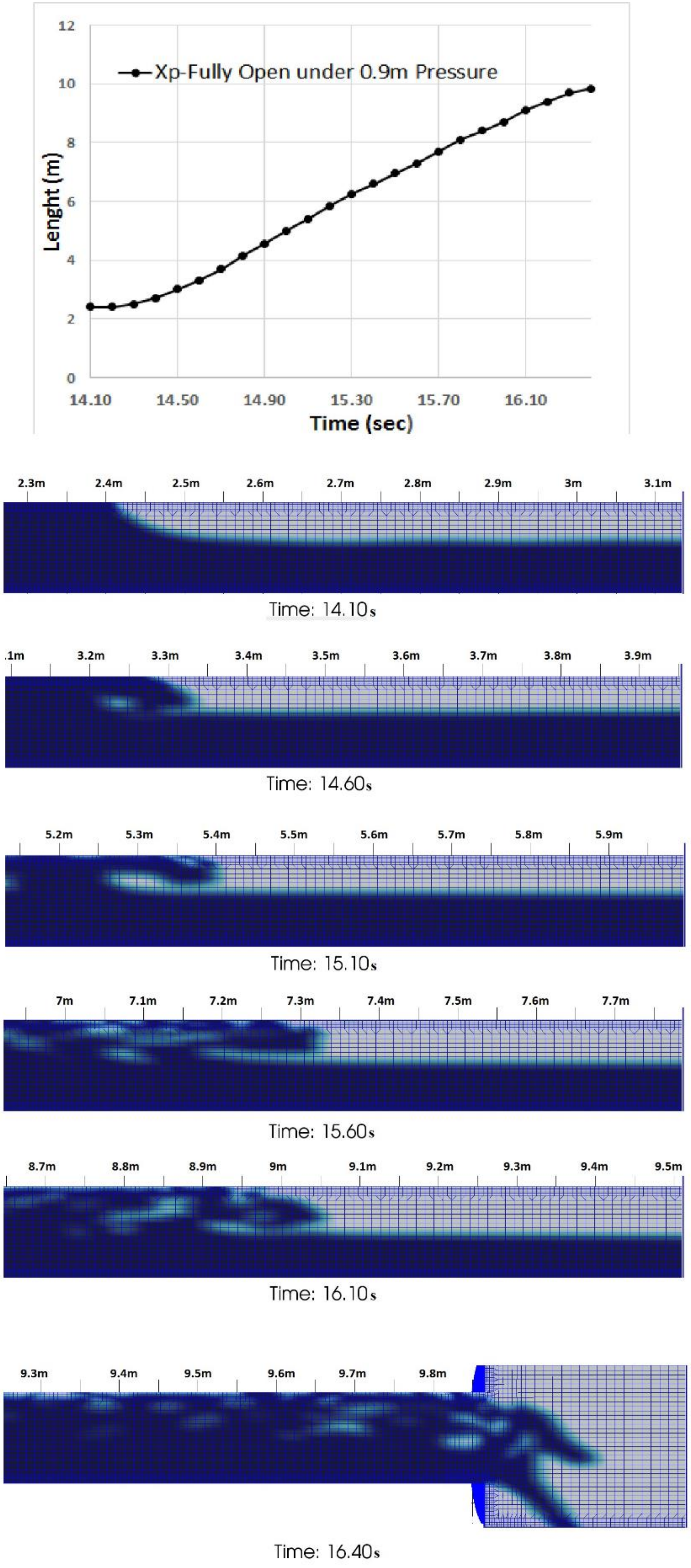

Figure 5. 23:The bore tracking for Fully open case under 0.914-m pressure head

The transformation a cavity flow to the bore is shown in Figure 5.24.

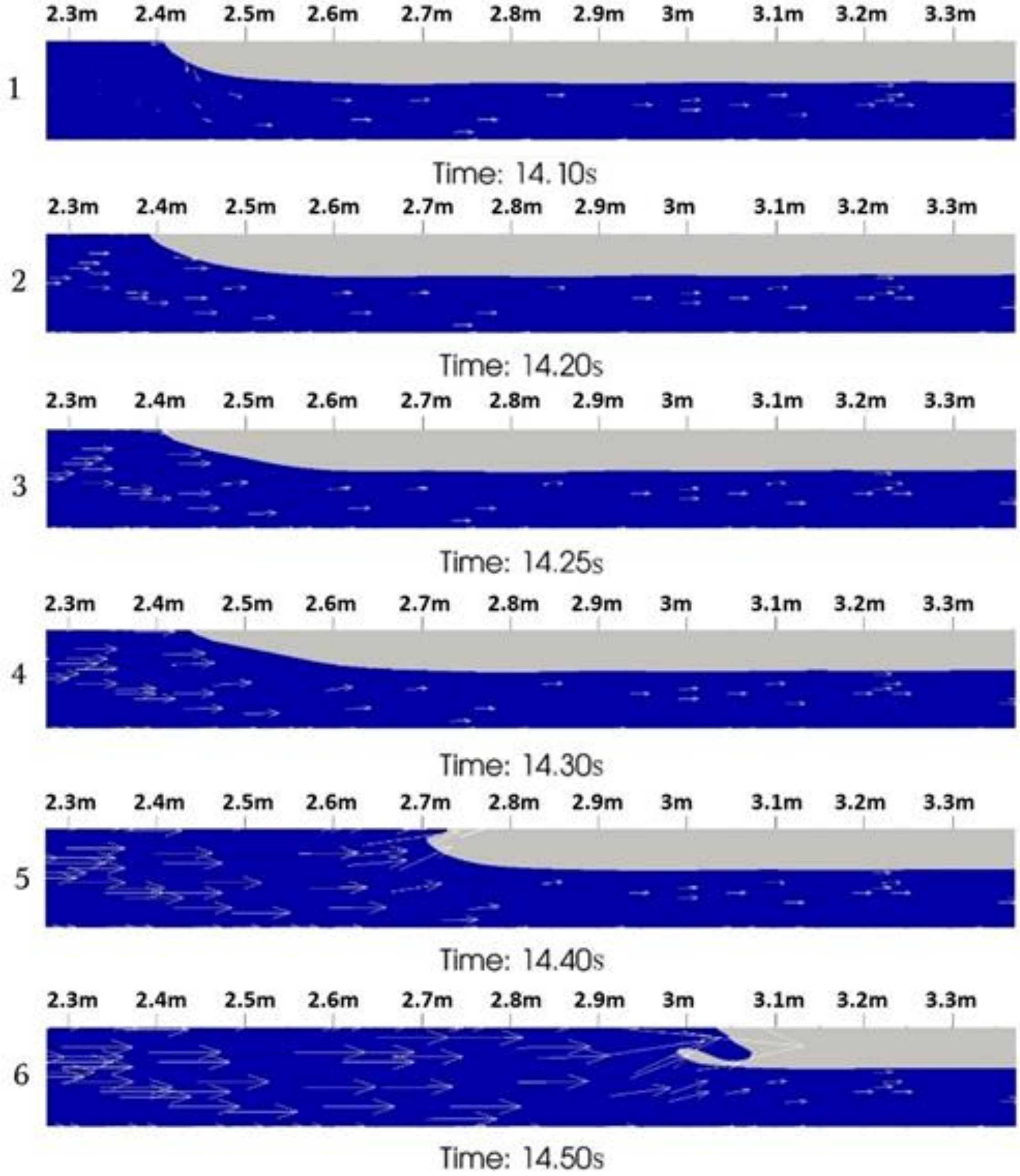

Figure 5. 24:Illustration of transform to bore in fully open case under 0.914-m pressure head

5.7 Large-scale Model

The large-scale pipes study was simply an effort to evaluate scale effects in the CFD simulation results by increasing every dimension (L, D, weir openings, pressure head at reservoir) by a factor of 10. Even though there is no means to compare these results with experimental data, this study at least allows to compare the results with the smaller scale simulations already developed. Only partially opened conditions were tested, involving weirs that created a gap with 200mm opening, 270mm opening and 380mm opening at the end of the pipeline in the OpenFOAM. The sequence of downstream and upstream gate openings was also unchanged.

Unlike the previous studies, the advance of the air cavity was allowed to vary along the pipeline. In this section of the research, rapid change in the pressure was allowed when the cavity reached 30%, 60% and 90% of the pipe length. Pressure head values supplied at the upstream end of the pipe varied between 3, 6 and 9 m. The maximum cavity intrusion in Table 5.10, entrapped air pocket volume in Table 5.11, and the percentage of air pocket volumes that caught in the pipe from the cavity in Table 5.12 are shown below.

Table 5. 10: The maximum cavity intrusion for large-scale models

	Air Cavity Maximum Intrusion Volume (m^3)			
Cavity Advance	Upstream Reservoir Pressure Head	Downstream Weir Opening		
		380 mm	270 mm	200 mm
27.4 m	3 m	3.021	1.995	1.233
	6 m	2.990	1.982	1.227
	9 m	2.978	1.976	1.227
54.9 m	3 m	5.795	3.888	2.399
	6 m	5.775	3.878	2.399
	9 m	5.769	3.878	2.399
82.3 m	3 m	8.556	5.737	3.560
	6 m	8.556	5.737	3.560
	9 m	8.556	5.737	3.560

Table 5. 11: Entrapped air pocket volume for large-scale models

	Entrapped Air Pocket Volume (m^3)			
Cavity Advance	Upstream Reservoir Pressure Head	Downstream Weir Opening		
		380 mm	270 mm	200 mm
27.4 m	3 m	NA	NA	0.85
	6 m	NA	1.11	0.89
	9 m	1.85	1.16	0.87
54.9 m	3 m	1.42	2.17	1.86
	6 m	2.60	2.83	1.75
	9 m	2.23	2.65	1.89
82.3 m	3 m	3.77	4.21	2.90
	6 m	4.52	4.31	2.77
	9 m	4.66	4.14	2.43

Table 5. 12: Percentage of Initial Cavity Volume Entrapped as an Air Pocket for large-scale models

	% of Initial Cavity Volume Entrapped as an Air Pocket			
Cavity Advance	Upstream Reservoir Pressure Head	Downstream Weir Opening		
		380 mm	270 mm	200 mm
27.4 m	3 m	NA	NA	69.2*
	6 m	NA	56.2	72.9
	9 m	62.2	58.9	71.0
54.9 m	3 m	24.5*	55.9*	77.8
	6 m	45.1*	73.1	72.8
	9 m	38.7	68.4	78.8
82.3 m	3 m	44.1*	73.4*	81.4
	6 m	52.8	75.1	77.9
	9 m	54.5	72.2	68.3

Comparing these results with the smaller scale results shown in Table 5.8, it appears that the percentage of the air cavity that becomes entrapped in air pockets is comparable, but in general slightly smaller for the case with a 380-mm opening. More investigation in scale effects in SFI occurrence is certainly needed. In the Table 5.12 results, the asterisk values illustrate the cases that the theoretical SFI threshold by Li and McCorquodale (1999) does not indicate pocket entrapment occurrence but CFD does.

Chapter 6

6. Conclusions and Future Work

Air pocket entrapment in stormwater systems is still a poorly understood phenomenon. Unsteady, two-phase flow conditions have complex features that can lead to air pocket entrapment, which in turn create operational problems such as structural damage, manhole lid displacement, geysering, etc. Using experimental results and numerical results, this investigation studied various characteristics of two-phase flows, including air pocket formation. By using an innovative apparatus that enabled the development of air cavities with varying thickness and a rapid filling with different flow rates various air pocket entrapment conditions were observed systematically. Higher pressure head values in the upstream reservoir were key to create varying inflow rates that pushed the initially present cavity out of the apparatus.

The experiments enabled the observation of varying air pocket entrapment volumes, multiple air pocket formation, as well a comparison between the air pocket shapes observed in experiments and numerical predictions. Experimental results indicated that when the air cavity thickness decreased, and the pressure head at the upstream reservoir increased, the likelihood of air pocket entrapment via SFI mechanism increased, which was consistent with previously published work. It was also shown that the percentage of air the air cavity volume that is entrapped into air pockets vary according to the upstream pressure head and air cavity thickness.

At the locations of air-pocket entrapments, just before the pipe-filling bore reached this locations, the air pressure pressed water underneath and increased local pocket thickness, clearly a three-dimensional phenomenon. This observation is agree with the definition of the mechanism of shear flow instabilities proposed by Hamam and McCorquodale in 1982. They described SFI as a process that creates interfacial disturbances until it results in air-pocket entrapment throughout the air-water interface.

Experimental results also indicated that the entrapped air pockets sometimes merged with each other and created one long and thin pocket. This is an interesting observation that was not previously reported, but creates further difficulties in evaluating the fate of entrapped air pockets. In some experimental conditions, there was not enough drag force to remove these pockets, and they remained in the apparatus as a long thin pocket at the pipe crown.

The numerical results CFD results indicated the ability of these tools to capture the occurrence of SFI. In most cases the CFD predictions of SFI occurrences agreed with experimental observations, but in few cases the predictions of SFI did not corresponded to actual SFI occurrences. This was particularly the case when the 38-mm weir was installed at the downstream end. However, CFD did agree well with theoretical predictions presented by Li and McCorquodale (1999) for SFI occurrence. Causes for these discrepancies between experimental and numerical and theoretical predictions of SFI should be the focus of future studies. However, in practical terms, a more conservative approach as to the occurrence of SFI would not be a negative factor for engineers and designers trying to avoid issues associated air pocket entrapments in actual sewer and tunnel systems.

Consistent to experimental observations, CFD modeling was able to predict a sequence of air pocket formation created by SFI, which was also predicted by Li and McCorquodale (1999). CFD was also able to predict the merging of air pockets, again agreeing with experimental observations. However the number of air pockets that were formed did not match experimental observations, nor the shape of entrapped air pockets predicted by the CFD tool matched the experimental observations. Air pocket predicted by CFD were thinner and longer than the ones observed in the apparatus. This also points to a future research need, possibly using other alternatives for turbulence modeling or other free surface interface tracking algorithms instead of the VOF method.

Future research could include methods to measure experimentally the volume of entrapped air created by SFI mechanisms, as well study scale effects in the SFI occurrence in experiments. Other air-water interactions leading to air pocket formation may still be uncovered by research, and this in turn will help design safer stormwater infrastructure. Finally, future research could also include field monitoring of actual sewer systems to determine the occurrence of SFI. Observations in these laboratory tests helped in finding signatures of air pocket entrapment, such as pressure spikes during rapid filling of conduits, which could infer occurrence of SFI in actual sewers.

Bibliography

Arai, K., & Yamamoto, K. (2003). Transient analysis of mixed free-surface-pressurized flows with modified slot model (Part 1: Computational model and experiment). *Proceedings of ASME FEDSM'03 4TH ASME_JSME Joint Fluids Engineering Conference*, 1–9.

Arai, K., & Yamamoto, K. (2003). Transient analysis of mixed free-surface-pressurized flows with modified slot model (part2: similarity law and eigenvalue problem), *5222*, 1–6.

Baines, B. W. D. (1991). Air Cavities as Gravity Currents on Slope. *Journal of Hydraulic Engineering, ASCE*, *117*(12), 1600–1615. https://doi.org/10.1061/(ASCE)0733-9429(1991)117:12(1600)

Baines, P. G., & Mitsudera, H. (1994). On the mechanism of shear flow instabilities. *Journal of Fluid Mechanics*, *276*(1), 327. https://doi.org/10.1017/S0022112094002582

Baines, W. . D. (1991). Cavities as gravity currents on slope, *117*(12), 1600–1615.

Bashiri-atrabi, H., Asce, S. M., Hosoda, T., & Shirai, H. (2016). Propagation of an Air-Water Interface from Pressurized to Free-Surface Flow in a Circular Pipe, *142*(12), 1–9. https://doi.org/10.1061/(ASCE)HY.1943-7900.0001200.

Batchelor, G. K. (1967). Batchelor 1967-An introduction to the fluid dynamics.pdf.

Benjamin, T. B. (1968). Gravity currents and related phenomena. *J. Fluid. Mech.*, *31*(02), 209–248. https://doi.org/10.1017/S0022112068000133

Chosie, C. D., Hatcher, T. M., & Vasconcelos, J. G. (2014). Experimental and Numerical Investigation on the Motion of Discrete Air Pockets in Pressurized Water Flows. *Journal of Hydraulic Engineering*, *140*(8), 04014038. https://doi.org/10.1061/(ASCE)HY.1943-7900.0000898

Greenshields, C. J. (2015). OpenFOAM User Guide. *OpenFOAM Foundation Ltd*, (December), 230.

Hamam, M. A., & McCorquodale, J. A. (1982). Transient conditions in the transition from gravity to surcharged sewer flow. *Canadian Journal of Civil Engineering*, *9*(2), 189–197. https://doi.org/10.1139/l82-022

Hirt, C. and B. D. Nichols. (1981). “Volume of Fluid (VOF) Method for the Dynamics of Free Boundaries.” *Journal of Computational Physics* 39 (1): 201–25.

Kordyban, E. (1990). Horizontal slug flow: a comparison of existing theories. *Journal of Fluids Engineering*, *112*(March), 1–10. https://doi.org/10.1115/1.2909372

Laanearu, J., Hou, D.Q. and, Tisseling, A. S. (2016). Experimental and analytical study of the air-water interface kinematics during filling and emptying of a horizontal pipeline, (April), 625–637.

Li, J. and, McCorquodale, A. (1999). Modeling Mixed Flow in Storm Sewers. *Journal of Hydraulic Engineering*, *125*(1983), 1170–1180.

Li, J., & McCorquadale, J. A. (1999). Low in, *125*(1983), 1170–1180.

Matsubara, C., Kuo, T., & Wu, H. (2013). Comparison of the Effects of k-ϵ, k-ω, and Zero Equation Models on Characterization of Turbulent Permeability of Porous Media. *Journal of Water Resource and Hydraulic Engineering*, *2*(2), 43–50. https://doi.org/10.1002/9781118869673

Muller, K. Z., Wang, J., & Vasconcelos, J. G. (2017). Water Displacement in Shafts and Geysering Created by Uncontrolled Air Pocket Releases. *Journal of Hydraulic Engineering*, *143*(10), 1–13. https://doi.org/10.1061/(ASCE)HY.1943-7900.0001362.

Muller, K. Z., Wang, J., Vasconcelos, J. G., & Asce, M. (2017). Water Displacement in Shafts and Geysering Created by Uncontrolled Air Pocket Releases. *Journal of Hydraulic Engineering*, *143*(10), 1–13. https://doi.org/10.1061/(ASCE)HY.1943-7900.0001362.

Reynolds, O. (1883). An Experimental Investigation of the Circumstances Which Determine Whether the Motion of Water Shall Be Direct or Sinuous, and of the Law of Resistance in Parallel Channels. *Royal Society Publishing*, *69*(2), 935–982. Retrieved from http://www.jstor.org/stable/109431

Svenungsson, J. (2016). Solving electric field using Maxwell ' s equations and compressibleInterFoam solver. *CFD with OpenSource Software*.

Vasconcelos, G.Jose, Wright, S. (2008). Rapid Flow Startup in Filled Horizontal Pipelines. *Journal of Hydraulic Engineering*, *134*(7), 1094–1100. https://doi.org/10.1061/(ASCE)0733-9429(2008)134

Vasconcelos, J. G., & Wright, S. J. (2006a). Mechanisms for Air Pocket Entrapment in Stormwater Storage Tunnels. *World Environmental and Water Resources Congress 2006*, *40856*(1999), 9–9. https://doi.org/10.1061/40856(200)9

Vasconcelos, J. G., & Wright, S. J. (2006b). Mechanisms for Air Pocket Entrapment in Stormwater Storage Tunnels. *World Environmental and Water Resources Congress 2006*, *40856*(1999), 9–9. https://doi.org/10.1061/40856(200)9

Wilkinson, D. L. (1982). Motion of air cavities in long horizontal ducts. *Journal of Fluid Mechanics*, *118*, 109. https://doi.org/10.1017/S0022112082000986

Townson, D. (1991). Free-Surface Hydraulics. London: CRC Press.

Svenungsson, Josefine. 2016. “Solving Electric Field Using Maxwell ' s Equations and CompressibleInterFoam Solver.” *CFD with OpenSource Software*.